A&A 491, 465–481 (2008)
DOI: 10.1051/0004-6361:200810724

Astronomy
&
Astrophysics

An unbiased measurement of the UV background and its evolution via the proximity effect in quasar spectra[⋆],[⋆⋆]

A. Dall'Aglio, L. Wisotzki, and G. Worseck

Astrophysikalisches Institut Potsdam, An der Sternwarte 16, 14482 Potsdam, Germany
e-mail: `adaglio@aip.de`

Received 31 July 2008 / Accepted 19 September 2008

ABSTRACT

We investigated a set of high-resolution ($R \sim 45\,000$), high signal-to-noise ($S/N \sim 70$) quasar spectra to search for the signature of the so-called proximity effect in the H I Lyα forest. The sample consists of 40 bright quasars with redshifts in the range $2.1 < z < 4.7$. Using the flux transmission statistic, we determined the redshift evolution of the H I effective optical depth in the Lyman forest between $2 \lesssim z \lesssim 4.5$, finding good agreement with previous measurements based on smaller samples. We also see the previously reported dip in $\tau_{\mathrm{eff}}(z)$ around redshift $z \sim 3.3$, but as the significance of that feature is only 2.6σ, we consider this detection tentative. Comparing the flux transmission near each quasar with what was expected from the overall trend of $\tau_{\mathrm{eff}}(z)$, we clearly detect the proximity effect not only in the combined quasar sample, but also towards each individual line of sight at high significance, albeit with varying strength. We quantify this strength using a simple prescription based on a fiducial value for the intensity of the metagalactic UV background (UVB) radiation field at 1 Ryd, multiplied by a free parameter that varies from QSO to QSO. The observed proximity effect strength distribution (PESD) is asymmetric, with an extended tail towards values corresponding to a weak effect. We demonstrate that this is not simply an effect of gravitational clustering around quasars, as the same asymmetry is already present in the PESD predicted for purely Poissonian variance in the absorption lines. We present the results of running the same analysis on simulated quasar spectra generated by a simple Monte-Carlo code. Comparing the simulated PESD with observations, we argue that the standard method of determining the UVB intensity J_{ν_0} by averaging over several lines of sight is heavily biased towards high values of J_{ν_0} because of the PESD asymmetry. Using instead the *mode* of the PESD provides an estimate of J_{ν_0} that is unbiased with respect to his effect. For our sample we get a modal value for the UVB intensity of $\log J_{\nu_0} = -21.51 \pm 0.15$ (in units of erg cm^{-2} s^{-1} Hz^{-1} sr^{-1}) for a median quasar redshift of 2.73. With J_{ν_0} fixed we then corrected τ_{eff} near each quasar for local ionisation and estimated the amount of excess H I absorption attributed to gravitational clustering. On scales of ~3 Mpc, only a small minority of quasars show substantial overdensities of up to a factor of a few in τ_{eff}; these are exactly the objects with the weakest proximity effect signatures. After removing those quasars residing in overdense regions, we redetermined the UVB intensity using a hybrid approach of sample averaging and statistical correction for the PESD asymmetry bias, arriving at $\log J_{\nu_0} = -21.46^{+0.14}_{-0.21}$. This is the most accurate measurement of J_{ν_0} to date. We present a new diagnostic based on the shape and width of the PESD that strongly supports our conclusion that there is no systematic overdensity bias for the proximity effect. This additional diagnostic breaks the otherwise unavoidable degeneracy of the proximity effect between UVB and overdensity. We then applied our hybrid approach to estimate the redshift evolution of the UVB intensity and found tentative evidence of a mild decrease in $\log J_{\nu_0}$ with increasing redshift, by a factor of ~0.4 from $z = 2$ to $z = 4$. Our results are in excellent agreement with earlier predictions for the evolving UVB intensity, and they also agree well with other methods of estimating the UVB intensity. In particular, our measured UVB evolution is much slower than the change in quasar space densities between $z = 4$ and $z = 2$, supporting the notion of a substantial contribution of star-forming galaxies to the UVB at high redshift.

Key words. cosmology: diffuse radiation – galaxies: intergalactic medium – galaxies: quasars: absorption lines

1. Introduction

High-resolution spectra of high-redshift, quasi-stellar objects (QSOs) show a plethora of narrow absorption lines from various species along their lines of sight through the intergalactic medium (IGM). Most absorption lines blueward of an Lyα emission line stem from the Lyα transition of intervening neutral hydrogen, giving rise to the Lyα forest (Sargent et al. 1980; Weymann et al. 1981; Rauch 1998). High-resolution spectra of the Lyα forest enabled a statistical analysis of the absorbers, as well as their physical properties (e.g. Kim et al. 2001; Schaye et al. 2003; Kim et al. 2004).

The vast majority of H I Lyα absorbers are optically thin to ionising photons and are thus kept highly photoionised by the metagalactic UV background (UVB) generated by the overall population of quasars and star-forming galaxies (Haardt & Madau 1996; Fardal et al. 1998; Haardt & Madau 2001). The UVB intensity at a given frequency is determined by the evolving population of UV sources, modified by cosmological expansion and absorption (e.g. Davé et al. 1999). It is important to determine the amplitude of the UVB and its spectral shape as a function of redshift in order to constrain the relative contributions of quasars and star-forming galaxies to the UVB, as well as to provide a key ingredient to numerical simulations of structure formation.

There are different ways to constrain the H I UVB photoionisation rate in the IGM. Assuming its spectral energy distribution it is possible to infer the UVB intensity at the Lyman limit J_{ν_0}.

[⋆] Based on data collected at the European Southern Observatory and obtained from the ESO Science Archive.

[⋆⋆] Appendix A is only available in electronic form at `http://www.aanda.org`

Article published by EDP Sciences

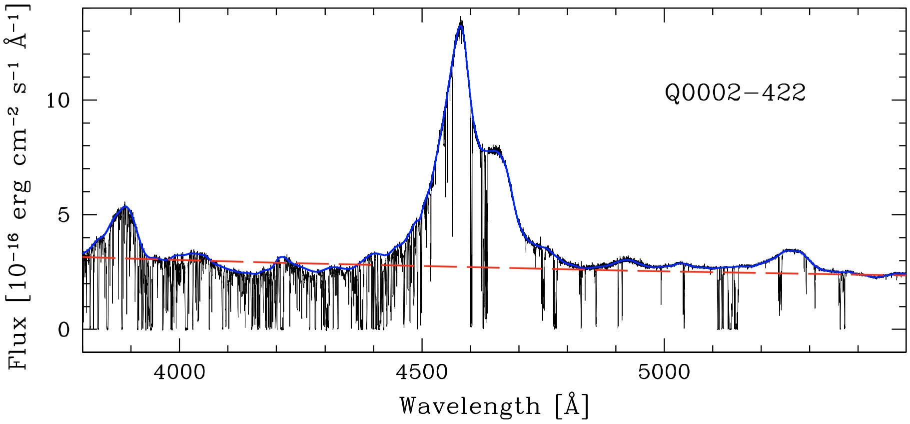

Fig. 1. A typical quasar spectrum from our sample (Q 0002−422 z = 2.768) together with the power law continuum fit (dashed red line) and the local continuum fit (blue line).

First, the UVB can be predicted by integrating the contributions of the observed source population. Given the luminosity functions of the sources, a characteristic intrinsic spectral energy distribution and the observed absorber distribution functions in the IGM, the amplitude and spectral shape of the UVB can be calculated numerically as the radiation is filtered by the IGM (Bechtold et al. 1987). In particular, comparing these models to observations provides constraints on the relative contributions of quasars (Haardt & Madau 1996; Fardal et al. 1998) and star-forming galaxies (Haardt & Madau 2001).

Furthermore, the H I photoionisation rate at $2 < z < 4$ has been constrained by matching the Lyα forest absorption and the IGM temperature evolution from numerical simulations of structure formation to observations (Rauch et al. 1997; Theuns et al. 1998; McDonald et al. 2000; Meiksin & White 2004; Tytler et al. 2004; Bolton et al. 2005; Kirkman et al. 2005; Jena et al. 2005).

A more direct approach to estimate the UVB photoionisation rate is based on the so-called proximity effect. In the vicinity of a luminous quasar the UV radiation field is expected to be enhanced, resulting in a statistical deficit of Lyα absorbers near the quasar compared to far away from it along the line of sight (Weymann et al. 1981; Carswell et al. 1982; Murdoch et al. 1986). Knowing the UV luminosity of the quasar, the deficit of lines (or generally Lyα opacity) yields an estimate of the UVB intensity at the H I Lyman limit (Carswell et al. 1987; Bajtlik et al. 1988). Traditionally, the proximity effect has been considered as a statistical effect and large samples of up to ∼100 quasars have been compiled to measure the mean UVB at $2 \lesssim z \lesssim 4$ (e.g. Bajtlik et al. 1988; Lu et al. 1991; Giallongo et al. 1996; Cooke et al. 1997; Scott et al. 2000; Liske & Williger 2001). Nevertheless, the proximity effect can also be detected towards individual quasars (e.g. Williger et al. 1994; Cristiani et al. 1995; Lu et al. 1996; Savaglio et al. 1997; Dall'Aglio et al. 2008).

Proximity effect analyses at different redshifts can constrain the redshift evolution of the UVB, showing that it broadly peaks at $z \sim 3$. The decrease in the UVB at $z < 2$ (Kulkarni & Fall 1993; Scott et al. 2002) and $z \gtrsim 4$ (Williger et al. 1994; Lu et al. 1996; Savaglio et al. 1997) is likely due to the declining space density of quasars (Haardt & Madau 1996; Fardal et al. 1998). Whereas the UVB evolution at low redshifts is sufficiently fast to be detectable within a single sample (Scott et al. 2002), there is presently little direct evidence of evolution within the redshift range $2 \lesssim z \lesssim 4$.

It is currently an open issue whether the measured UVB at $z \lesssim 3$ is consistent with the integrated emission of quasars, or whether a significant share of ionising photons has to be provided by star-forming galaxies (e.g. Madau et al. 1999; Sokasian et al. 2003; Schirber & Bullock 2003; Hunt et al. 2004). One difficulty lies in the fact that the UVB estimates via the proximity effect are subject to several systematic uncertainties, all of which can lead to an overestimate of the inferred UV background:

1. *Quasar variability*: the size of the proximity effect zone scales as the average quasar luminosity over the photoionisation equilibrium timescale in the IGM (∼10^4 yr). Quasar variability on shorter timescales will tend to overestimate the UVB due to Malmquist bias in the selected quasar samples (Schirber et al. 2004). It is not known how important this effect is in practice.
2. *Underestimated quasar redshifts*: quasar emission redshifts determined from broad high-ionisation lines are likely underestimated (e.g. Gaskell 1982; Richards et al. 2002), causing the UVB to be overestimated by a factor ∼3 (Espey 1993). However, this effect can be largely avoided by using low-ionisation lines to determine systemic redshifts.
3. *Overdense environment*: in the standard ionisation model of the proximity effect (Bajtlik et al. 1988), the Lyα forest line density is extrapolated into the quasar vicinity, assuming that the matter distribution is not altered by the presence of the QSO. If quasars typically reside in high intrinsic overdensities instead, the UVB will be overestimated by a factor of up to ∼3 (Loeb & Eisenstein 1995). Conversely, the disagreement between the UVB estimates from the proximity effect and those obtained by matching simulations to the mean Lyα forest absorption has recently been used as an argument that quasars are surrounded by substantial overdensities (Rollinde et al. 2005; Guimarães et al. 2007; Faucher-Giguère et al. 2008b).

In the present paper we pursue a new approach to employ the proximity effect as a tool to investigate the UVB, based on measuring its signature towards individual QSO sight lines. We demonstrated recently (Dall'Aglio et al. 2008, hereafter Paper I) that indeed essentially all quasars show this signature, even at relatively low spectral resolution. Here we follow up on this finding, now based exclusively on high resolution, high *S/N* quasar spectra. The plan of the paper is as follows. We begin with a brief description of our spectroscopic data (Sect. 2). In Sect. 3 we explain the Monte Carlo simulations used to assess uncertainties and to interpret the observed proximity effect strength distribution. We then determine the redshift evolution of the effective optical depth in the Lyα forest in Sect. 4, followed by a comparison between the two most commonly adopted methods of revealing the proximity effect in Sect. 5. We very briefly report on the analysis of the combined QSO sample in Sect. 6. In Sect. 7 we investigate the proximity effect in individual sightlines, showing that the traditional sample-combining method is biased. We then estimate the excess Lyα absorption near quasars (Sect. 8), and use this to constrain the redshift evolution of the UVB (Sect. 9). We present our conclusions in Sect. 10.

Throughout this paper we assume a flat universe with Hubble constant $H_0 = 70$ km s^{-1} Mpc^{-1} and density parameters $(\Omega_\mathrm{m}, \Omega_\Lambda) = (0.3, 0.7)$. All distances are expressed in physical units.

2. Data

2.1. Sample description and data reduction

The sample consists of 40 quasar sight lines observed with the UV-Visual Echelle Spectrograph (UVES, Dekker et al. 2000) at VLT/UT2 on Cerro Paranal, Chile. All 40 spectra were taken from the ESO archive and are publicly available. We selected the QSO sample based on the following criteria: (i) a minimum of 10 exposures; and (ii) a complete or nearly complete coverage of the Lyα forest region especially close to the quasar. Table 1 lists the complete sample of quasars with adopted redshifts (Sect. 2.4) and quasar luminosities at the Lyman limit (Sect. 2.3).

The data were reduced within the ECHELLE/UVES environment (version 2.2) of the software package MIDAS and following the procedures described in Kim et al. (2004). After the bias and inter-order background subtraction from each science frame, an optimal extraction of the spectrum was performed, order by order, assuming a Gaussian distribution along the spatial direction. The sky was estimated and subtracted together with the Gaussian fit, maximising the quality of the extracted spectrum (e.g. Kim et al. 2001). Cosmic rays were identified and removed using a median filter. The wavelength calibration was performed with the available ThAr lamp frames. Relative flux calibration was performed using the master-response functions publicly available on the ESO website and accounting for different airmasses. This allowed us to place our spectra onto a relative flux scale reasonably well, while the absolute scale had to be tied to external photometry (Sect. 2.2). In each final coadded spectrum the individual extractions were weighed corresponding to their *S/N* and re-sampled on 0.05 Å bins. The resolving power is ~45 000 in the regions of interest, corresponding to a velocity resolution of ~6 km s^{-1} (FWHM). The wavelengths in the final spectra are vacuum heliocentric, and the fluxes are corrected for galactic reddening. An example of a final spectrum as well as our continuum definitions (Sect. 2.3) is shown in Fig. 1.

2.2. Quasar magnitudes

Table 1 provides our adopted apparent magnitudes and Lyman limit fluxes. The photometric data were collected from various sources, in particular SDSS, Véron-Cetty & Véron (2006), Rollinde et al. (2005), Cooke et al. (1997), Ellison et al. (2005), and Paper I. Where more than one measurement was available, the data were consistent to within $\sigma_\mathrm{m} < 0.1$ mag. Note that while knowledge of the Lyman limit luminosity is indispensable for the quantitative interpretation of the proximity effect, even perfectly simultaneous high-*S/N* photometry would not account for the effects of quasar variability averaged over the photoionisation time scale. By randomly changing the flux scale of some objects by up to 20% we confirmed that our conclusions concerning the proximity effect are not affected by photometric uncertainties.

Table 1. List of analysed QSOs, ordered by redshift.

QSO	Mag	Filter	*S/N*	$f_{\nu 0}^{\ddagger}$	$\log L_{\nu 0}^{\star}$	$z_\mathrm{em}{}^{\dagger}$
HE 1341−1020	17.1	*B*	70	139	31.17	2.137
Q 0122−380	16.7	*B*	60	291	31.51	2.192
PKS 1448−232	17.0	*V*	70	282	31.50	2.222
PKS 0237−233	16.6	*V*	100	750	31.93	2.224
HE 0001−2340	16.7	*V*	60	403	31.68	2.278
HE 1122−1648^a	16.5	*V*	120	866	32.05	2.407
Q 0109−3518	16.4	*B*	70	404	31.72	2.406
HE 2217−2818	16.0	*V*	80	796	32.02	2.414
Q 0329−385	17.0	*V*	50	226	31.48	2.437 ^{b}
HE 1158−1843	16.9	*V*	60	268	31.56	2.459
Q 2206−1958	17.3	*V*	70	255	31.57	2.567
Q 1232+0815	18.4	*r*	50	055	30.91	2.575
HE 1347−2457	16.8	*B*	60	772	32.06	2.615
HS 1140+2711^a	16.7	*r*	80	581	31.94	2.628
Q 0453−423	17.1	*V*	70	168	31.41	2.664
PKS 0329−255	17.1	*V*	50	243	31.58	2.706
Q 1151+0651	18.1	*r*	50	100	31.21	2.758
Q 0002−422	17.2	*V*	60	346	31.76	2.769
Q 0913+0715	17.8	*r*	60	181	31.48	2.788
HE 0151−4326	17.2	*B*	70	499	31.92	2.787
Q 1409+095	18.6	*r*	40	067	31.06	2.843
HE 2347−4342	16.7	*V*	100	630	32.05	2.886
Q 1223+1753	18.1	*r*	40	794	31.16	2.955
Q 0216+080^a	18.1	*V*	40	084	31.20	2.996
HE 2243−6031	16.4	*V*	100	776	32.17	3.012
CTQ 0247	17.4	*V*	70	239	31.66	3.025
HE 0940−1050	16.4	*V*	50	691	32.13	3.089
Q 0420−388	16.9	*V*	100	426	31.93	3.120
CTQ 0460	17.5	*V*	60	281	31.76	3.141
Q 2139−4434	17.7	*V*	40	117	31.39	3.207
Q 0347−3819	17.7	*V*	60	213	31.66	3.229
PKS 2126−158	17.0	*V*	60	380	31.92	3.285^c
Q 1209+0919	18.6	*r*	40	120	31.42	3.291^c
Q 0055−2659	17.5	*V*	60	245	31.81	3.665^c
Q 1249−0159^a	18.6	*g*	60	071	31.27	3.668
Q 1621−0042	17.3	*r*	70	307	31.91	3.709
Q 1317−0507	17.7	*R*	50	084	31.35	3.719
PKS 2000−330^a	17.0	*V*	60	178	31.69	3.786
BR 1202−0725	17.8	*R*	100	460	32.24	4.697
Q 1451−1512	17.3	*I*	60	332	32.12	4.766

‡ Lyman limit flux in units of μJy with uncertainties around 7%.

★ Lyman limit luminosities in units of erg s^{-1} Hz^{-1} with uncertainties of the order of $\sigma_{\log L_{\nu 0}} \simeq^{+0.05}_{-0.1}$ dex.

† Systemic redshift estimated from Si II+O I at $\lambda_\mathrm{rest} = 1305.77$ Å (Morton 2003). Redshift uncertainty is $\sigma_z = 0.003$.

[a] Gaps in the spectral range of the Lyα forest.

[b] Redshift measured from C IV emission line and corrected according to Richards et al. (2002).

[c] Redshift taken from Paper I.

2.3. Continuum definition

In order to search for the proximity effect, we needed to convert the quasar spectra into continuum-rectified transmission spectra. We also needed to know the quasar flux at the Lyman limit. To achieve this we determined two types of continua: (i) a global power law ($f_\nu \propto \nu^\alpha$), excluding emission and absorption regions, used to estimate the quasar flux at the Lyman limit; and (ii) a more local estimate that also includes the broad emission lines as a quasi-continuum, used to compute the transmission spectrum. We constrained the Lyman limit flux via a power law continuum fit since in most cases this wavelength is either not covered by the observations or is located in the far blue range of the spectrum where the *S/N* significantly drops.

We developed an algorithm to automatically fit the local continuum, building on the work by Young et al. (1979) and

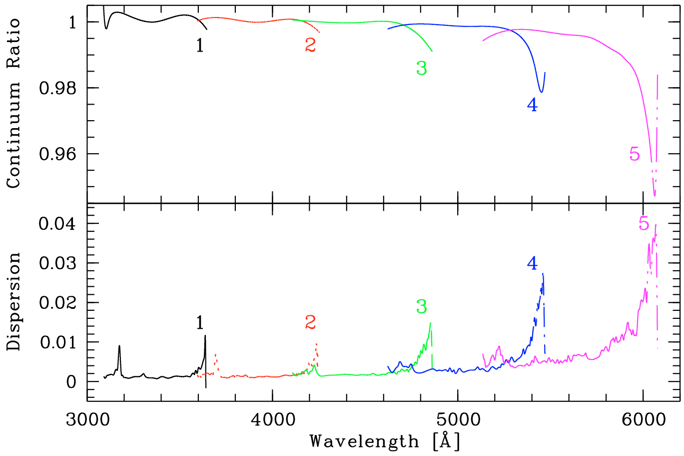

Fig. 2. *Top panel*: average ratio between the fitted and input continuum for the five sets of 500 simulated QSOs at $z = 2.0, 2.5, 3.0, 3.5, 4.0$ with $S/N = 70$, denoted with numbers 1, 2, 3, 4 and 5 respectively. *Bottom panel*: standard deviation profiles relative to the above systematic bias.

Carswell et al. (1982). A cubic spline was interpolated on adaptive intervals along the spectrum. The fixpoints for the spline interpolation were chosen starting from a regular sampling of the spectrum with a binning that becomes finer whenever the slope of the computed continuum exceeds a given threshold. This was done in order to better reproduce the wings of emission lines.

To assess the continuum uncertainties we proceeded in the same way as described in Paper I. With the help of Monte Carlo simulations we computed the average ratio between the recovered and the input continua at different redshifts. The results are presented in Fig. 2. The top panel shows the mean systematic error of the fitted continuum with respect to the input continuum for five different redshifts. The bottom panel presents the intrinsic uncertainties of the continuum. Due to the high resolution and the high *S/N* of the spectra, the statistical error associated with continuum placement is limited to a few percent at most in the Lyα line wing. The automatically fitted continuum was corrected for the systematic bias and used to compute the transmission $T = F_{\rm qso}/F_{\rm cont}$.

Regarding the Lyman limit fluxes, the uncertainties are of the order of 7%, dominated by the somewhat subjective choice of the continuum wavelength ranges redward of the Lyα emission used to fit the power laws.

2.4. Systemic quasar redshift

The spectral range covered by the UVES observations can maximally extend from ~3000 to ~10 000 Å. However, not all QSOs have such wide wavelength coverage. Most of them extend far enough to the red of Lyα to allow the detection of several emission lines (Si II + O I, C II, Si IV + O IV], C IV) from which a redshift can be measured. Several authors (e.g. Gaskell 1982; Tytler & Fan 1992; Richards et al. 2002) pointed out the existence of a systematic shift between high and low ionisation lines attributed to the relative motion of gas near the AGN. In order to measure a redshift as close as possible to the systemic one, we used low-ionisation lines if these were available. In almost all cases we adopted Si II + O I measurements for the final emission redshift, as listed in Table 1. For four objects (PKS 2126−158, Q 0329−385, Q 1209+0919 and Q 0055−2659) this was not possible due to either a non-detection of these lines or lack of wavelength coverage. For PKS 2126−158, Q 1209+0919 and Q 0055−2659 we adopted the redshifts based on Si II + O I from the low-resolution spectra in Paper I, while for Q 0329−385 we could only take the C IV based redshift and corrected it for the mean systematic shift determined by Richards et al. (2002).

3. Monte Carlo simulations of artificial spectra

A deeper understanding of statistical and systematic effects contributing to the proximity effect signature is made possible by comparing observations with simulated spectra. Typically, numerical 3D simulations are successful in reproducing the properties of the Lyα forest at any redshift. However, such computations are very time consuming and their major shortcoming is the limited redshift coverage of the simulated sight lines, especially at high resolution.

We developed a straightforward Monte Carlo code to generate synthetic spectra and employed the simulations for three main purposes. First, to estimate the influence of the quasar continuum placement in the spectra (Sect. 2.3); then to compute the line-of-sight variations in the evolution of the optical depth in the Lyα forest (Sect. 4); and finally to study the influence of the fact that only a finite number of absorbers contributes to the measured optical depth (Sect. 5.3).

The procedure used to generate synthetic spectra is based on the assumption that the Lyα forest is well represented by three observed distributions:

1. The line number density distribution, approximated by a power law of the form $dn/dz \propto (1+z)^{\gamma}$ where γ will be measured in Sect. 4.
2. The column density distribution, given by $f(N_{\rm H\,I}) \propto N_{\rm H\,I}^{-\beta}$ where the slope is $\beta \simeq 1.5$ (Kim et al. 2001).
3. The Doppler parameter distribution, given by $dn/db \propto b^{-5}\exp\left[-b_{\sigma}^{4}/b^{4}\right]$ where $b_{\sigma} \simeq 24$ km s^{-1} (Kim et al. 2001).

The simulated absorbers have column densities within the range $10^{12} < N_{\rm H\,I} < 10^{18}$ cm^{-2} and Doppler parameters between $10 < b < 100$ km s^{-1}. The slope of the column density distribution was fixed to $\beta = 1.5$.

For our purposes these approximations are sufficient to yield the accuracy we need in the following analysis. Every simulated sight line was populated with absorption features drawn from the above distributions until the computed effective optical depth was consistent with its evolution presented in Sect. 4. Once the simulated transmission was computed, an artificial quasar spectral energy distribution, including emission lines of varying strengths and widths, was generated via the principal components method described by Suzuki (2006) and already employed in Paper I. Gaussian noise was added to the final quasar spectrum, in order to match the *S/N* level of our observed objects.

4. Evolution of the Lyα effective optical depth

The H I effective optical depth is related to the mean transmission as $\tau_{\rm eff} \equiv -\ln\langle T\rangle \equiv -\ln\langle e^{-\tau_{\rm H\,I}}\rangle$, where $\langle\ \rangle$ indicates the average over predefined redshift intervals. Note that the effective optical depth is defined as the negative logarithm of the average pixel by pixel transmission, and not as the average value of the pixel by pixel optical depth in a given redshift interval. Its redshift evolution (Zuo 1993) is usually well represented by a power law

$$\tau_{\rm eff} = \tau_0 (1+z)^{\gamma+1}. \tag{1}$$

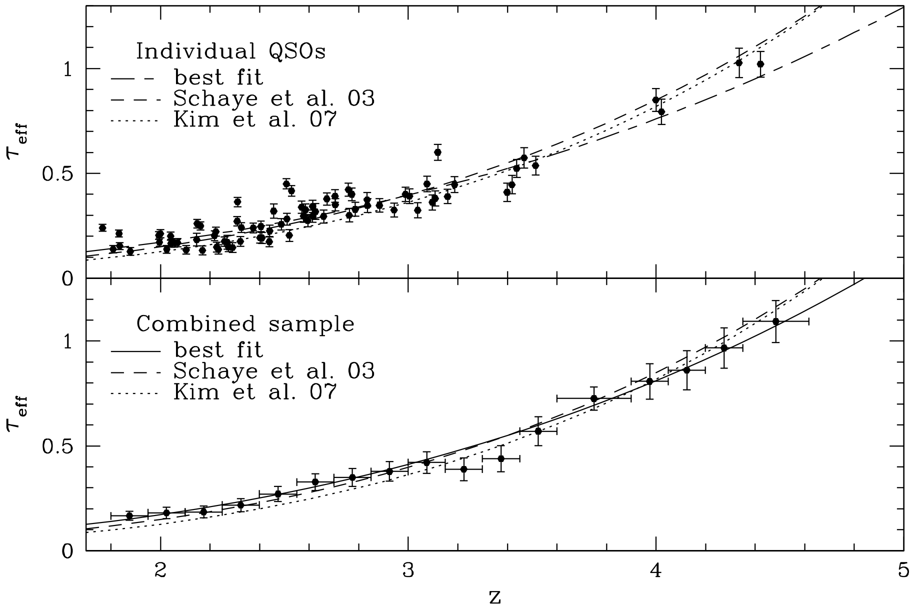

Fig. 3. Observed effective optical depth as a function of redshift after removal of pixels contaminated by Lyα absorption lines with damping wings, Ly limit systems and the proximity effect. Measurements from each individual quasar are shown *the lower panel*. The solid curve shows the power law least-squares fit to the data while the dashed curve indicates the evolution of the Lyα optical depth fitted by Schaye et al. (2003) and the dotted line that by Kim et al. (2007).

Table 2. Effective optical depth in the Lyα forest of our combined QSO sample.

$\langle z \rangle$	Δz	$\tau_{\rm eff}$	$\sigma_{\tau_{\rm eff}}$
1.874	0.15	0.166	0.021
2.024	0.15	0.180	0.026
2.174	0.15	0.185	0.028
2.324	0.15	0.217	0.031
2.474	0.15	0.270	0.035
2.624	0.15	0.327	0.040
2.774	0.15	0.349	0.042
2.924	0.15	0.378	0.046
3.074	0.15	0.420	0.051
3.224	0.15	0.388	0.054
3.374	0.15	0.439	0.061
3.524	0.15	0.569	0.068
3.749	0.30	0.726	0.054
3.974	0.15	0.807	0.084
4.124	0.15	0.861	0.093
4.274	0.15	0.967	0.095
4.483	0.27	1.093	0.099

We explored two methods of determining the evolution of $\tau_{\rm eff}$ with redshift.

In the first approach each Lyα forest spectrum was divided into two redshift intervals, each covering the same redshift path length to sample the increasing opacity along single sight lines. The upper panel of Fig. 3 shows the results obtained using all those pixels in the Lyα forest range decontaminated from damped Lyα or Lyman limit systems (DLAs and LLSs respectively) and the proximity effect region ($\Delta v < 5000$ km s^{-1} were excluded).

The second approach consists of measuring the mean $\tau_{\rm eff}$ in the forest of all quasars intersecting a particular redshift slice ($\Delta z = 0.15$). The results are shown in Table 2 and in the lower panel of Fig. 3, yielding best-fit values of $(\log \tau_0, \gamma) = (-2.21 \pm 0.09, 2.04 \pm 0.17)$.

For both approaches the uncertainties in the effective optical depth, $\sigma_{\tau_{\rm eff}}$, quantify the amount of variance between the individual lines of sight for the considered redshift range.

In Fig. 3 we present the results from the two approaches in comparison to the evolution of the Lyα optical depth as measured by Schaye et al. (2003), using a similar technique on 19 QSO spectra taken with UVES and HIRES and the fit by Kim et al. (2007) combining 18 UVES spectra. Our results agree well with both Schaye et al. (2003) and Kim et al. (2007) fits. There is less agreement at high redshift, probably due to the limited number of QSOs at $z > 3.6$, but our results are formally consistent within the errors.

Although both panels use the same data, these were combined in different ways and thus return slightly different results. It is clear from the top panel that the first method suffers from a lack of data points in the range $3.6 < z < 4$, leading us to slightly underestimate the effective optical depth at high redshift. The second approach significantly reduces the scatter caused by cosmic variance as already pointed out by Kim et al. (2002). It is also in good agreement with literature estimates. Therefore we adopt the best-fit parameters from the second method to describe the redshift dependence of the normalised effective optical depth in our quasar spectra.

In the bottom panel of Fig. 3 we identify a marginally significant departure of $\tau_{\rm eff}$ from the power law evolution in the redshift range $3.2 \lesssim z \lesssim 3.4$. This feature, first discovered by Bernardi et al. (2003) using SDSS quasar spectra (but see McDonald et al. 2005), has been been interpreted to be a result of one or more of the following effects: (i) a change in the IGM temperature; (ii) a change in the free electron number density; or (iii) an enhancement in the UV background possibly connected to He II reionisation. Recently, Faucher-Giguère et al. (2008c) found the same dip in $\tau_{\rm eff}(z)$ using a sample of ESI and HIRES spectra. In the light of this debate and using a completely independent data sample, we confirm the detection of this feature. We note, however, that its significance is only 2.6σ (two pixels with each 1.8σ), so the detection can be called no more than tentative.

5. Methods of quantifying the proximity effect

The direct signature of an enhanced ionisation field near bright quasars is a reduction of the neutral hydrogen fraction on a physical scale of several Mpc. Two principal techniques to detect it have been developed in the last two decades, which we briefly review in the following subsections.

5.1. Flux transmission statistics

The method used in this work to reveal the proximity effect along single lines of sight is based on the comparison between the observed effective optical depth and the expected one in the Lyα forest (Liske & Williger 2001). Approaching the quasar systemic redshift, the photoionisation rate of the source starts to dominate over the UVB. This effect leads to an enhancement in H^+ relative to H^0, reducing the opacity of absorbers close to the QSOs. This influence modifies the effective optical depth, which becomes

$$\tau_{\text{eff}} = \tau_0(1+z)^{\gamma+1}(1+\omega)^{1-\beta} \tag{2}$$

(Liske & Williger 2001) where β is the slope in the column density distribution and ω is the ratio between the quasar and background photoionisation rates.

Following the assumptions outlined in Bajtlik et al. (1988) to compute ω, we get

$$\omega(z) = \frac{f_\nu(\lambda_0(1+z))}{4\pi J_{\nu_0}} \frac{1}{(1+z)} \left(\frac{d_{\rm L}(z_{\rm q},0)}{d_{\rm L}(z_{\rm q},z)}\right)^2 \tag{3}$$

with z as the redshift along the LOS such that $z < z_{\rm q}$, $d_{\rm L}(z_{\rm q}, 0)$ the luminosity distance of the QSO to the observer, and $d_{\rm L}(z_{\rm q}, z)$ as seen at any foreground redshift in the LOS.

Equation (3) implies that the spectral shape of the QSO and the background are approximately the same around 1 Ryd, which might not be exactely true. Assuming a quasar spectral shape $f_\nu \propto \nu^\alpha$, with $\alpha_{\rm q} \simeq -0.5$ (Vanden Berk et al. 2001) and taking a background spectral index of $\alpha_{\rm b} \simeq -1.4$ (Agafonova et al. 2005), the resulting scale of ω is shifted by ~0.1 dex. However, there may be an indication of a break in the spectral slope of quasars around the Lyman limit (Telfer et al. 2002). Such a break would make the quasar spectrum more similar again to that of the background, reducing the effect on ω.

We adopt the following notation: the ratio of the observed optical depth to the one expected in the Lyα forest, or the *normalised effective optical depth* ξ, is given by

$$\xi = \frac{\tau_{\text{eff}}}{\tau_0(1+z)^{\gamma+1}} = (1+\omega)^{1-\beta}. \tag{4}$$

with the parameters ($\log \tau_0, \gamma$) measured in Sect. 4.

The proximity effect is apparent as a decrease in the normalised optical depth below unity as $\omega \to \infty$, i.e. towards the quasar. We make use of this technique, first to detect the proximity effect on our combined sample of quasars (Sect. 6), then towards single lines of sight (Sect. 7) and finally to assess the dependence of the measured UV background on redshift and overdensities (Sect. 9).

5.2. Line counting

Counting absorption lines stronger than a given threshold is historically the first technique used to measure the deficit of absorption near high redshift quasars. Typically represented by a Voigt profile, each absorption line has to be fitted and associated with a set of parameters ($N_{\text{H}\,\text{I}}, z, b$) describing its column density, redshift, and Doppler parameter, respectively. At medium resolution only the equivalent width can be measured. Several authors (e.g., Giallongo et al. 1996; Scott et al. 2000) used this approach to detect the proximity effect and to measure the UV background on combined samples of QSOs with the formalism introduced by Bajtlik et al. (1988). It is clear that at low spectral resolution, line counting is vastly inferior to the flux transmisson statistic because of line blending. On the other hand, at the high resolution of UVES and similar instruments, line counting could still be a reasonable approach. We therefore conducted a performance comparison of the two techniques, following the prescription in Sect. 3. We simulated the Lyα forest of a quasar at redshift $z = 3$, obtaining not only the spectrum but also keeping the *complete* line list. We repeated this step to create 500 independent simulated spectra.

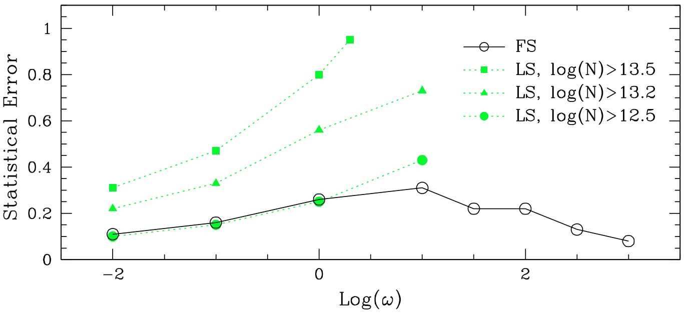

Fig. 4. Statistical errors associated with individual lines of sight using the line statistic (LS) and the flux statistic (FS) method. The different column density thresholds represent the completeness limits from Scott et al. (2000) and Hu et al. (1995) (solid squares and triangles, respectively). The filled circles show the level of uncertainty if the line list were complete up to the minimum column density at our resolution and *S/N*.

The principal limitation of the absorption line fitting approach is line blending, leading to incompleteness of weak lines at low column densities. Even at high resolution where lines with $\log N_{\text{H}\,\text{I}} \simeq 12.5$ are detectable, the completeness is <25% for column densities $\log N_{\text{H}\,\text{I}} < 13.2$ (Hu et al. 1995). Another problem in fitting absorption lines is that there is no unique solution, and much is left to the experience and ability of the scientist/software code in finding a *good* fit. For our simulation study we employed the code AUTOVP[1] to fully automatically fit an array of absorption lines to each spectrum. The proximity effect signature is then a decrease in the number density of lines N relative to that expected for the redshift. Thus we can define an alternative quantity

$$\xi' = \frac{N}{N_0} = (1+\omega)^{1-\beta}, \tag{5}$$

which again is expected to decrease from unity to zero as ω increases. We measured ξ (using the flux transmission statistic) and ξ' (from the automated line counts, adopting different column density thresholds) for all 500 simulated spectra, and computed mean and dispersion values for several bins of $\log \omega$.

Figure 4 presents the results of this study, showing the standard deviation of ξ or ξ', i.e. the statistical error of the measurement for a single line of sight, as a function of ω (approaching the quasar). For a realistic completeness limit in column density $\log N_{\text{H}\,\text{I}} > 13$, the flux transmission approach is always more sensitive than line counting. In the unrealistic ideal case where we used the true input line lists, the two methods are equivalent at low ω, but even then the line counting approach fails in probing ξ' very close to the emission redshift of the quasar. This can easily be understood as the quasar radiation reduces the column densities by a factor $1 + \omega$; thus, close to the quasar, where $\omega \gtrsim 100$, original column densities of $\log N_{\text{H}\,\text{I}} \gtrsim 15$ are needed to produce a detectable absorption line. Such absorbers are very rare, which leads to increased uncertainties.

---

[1] Developed by Davé: `http://ursa.as.arizona.edu/~rad`

We conclude that line counting is less sensitive to the expected proximity effect signature than the flux transmission method, even at high spectral resolution, and all our results will be based exclusively on the flux transmission technique.

5.3. Poissonian variance between lines of sight

At the spectral resolution in our sample, the major source of uncertainty is due to the variation in the number of absorption features along individual lines of sight. The probability of finding or not finding an absorption line at a given redshift is to first approximation a Poissonian process which can be easily modelled by our Monte Carlo simulations. While a full accounting of the expected effects of cosmic variance due to the large-scale structure of the IGM would require cosmological 3D simulations, it is actually useful to start with the Poissonian approximation, as it allows us to appreciate to what extent the observed level of variance is consistent with pure Poisson noise.

Equation (3) shows that ω depends on the redshift and luminosity of the quasar, implying that each QSO will have its own particular $\log\omega$ scale. Consequently, in a fixed $\log\omega$ interval the influence of Poisson noise will vary from line of sight to line of sight, since the corresponding redshift range in the Lyα forest is determined by the quasar emission redshift and its Lyman limit luminosity. Therefore, the distribution of the normalised optical depth ξ as a function of $\log\omega$ will depend on (i) Poisson noise; (ii) quasar redshift; and (iii) quasar luminosity.

We studied how the distribution of ξ is affected by different UV radiation fields (i.e. in different $\log\omega$ bins) at a given redshift. We computed the standard deviation σ given by

$$\sigma^2 = \int (\xi - \mu)^2 \, P(\xi) \, \mathrm{d}\xi \tag{6}$$

where $P(\xi)$ describes the probability density function of ξ estimated using our mock catalogue of sight lines as displayed in Fig. 5, and μ is its mean value. For illustration purposes, we assumed a quasar at redshift $z = 3$ and luminosity $\log L_{\nu_0} = 31.5$ with a binning of $\Delta\log\omega = 1$. Each panel displays how Poisson noise affects a different portion of the Lyα forest according to the quasar properties, i.e. for different values of ω. The final error bars in the proximity effect analysis are a composition of the following three effects, ordered by descending relative importance: (i) the standard deviation computed above; (ii) the continuum uncertainties (Sect. 2.3); and (iii) the intrinsic noise present in the spectrum. The Poisson noise in the placement of lines dominates the total error. Continuum uncertainties and the intrinsic noise are almost negligible.

6. The proximity effect in the combined sample of quasars

We first present briefly the evidence of the proximity effect in the traditional way, as a signal in the combined full sample of QSOs. The result is displayed in Fig. 6. As expected, the normalised effective optical depth ξ starts at unity for $\omega \ll 1$ and then goes down to zero for $\omega \gg 1$. In the definition of ω (Eq. (3)) we had to assume a fiducial value of the UVB intensity, $J^\star = 10^{-21}\,\mathrm{erg\,cm^{-2}\,s^{-1}\,Hz^{-1}\,sr^{-1}}$. This uniquely converts the redshift scale into an ω scale. We defined a regularly spaced grid along the $\log\omega$ axis and in each bin we determined the average transmission and effective optical depth values, and using Eq. (4) the corresponding values of ξ. We then modelled the decrease in ξ with $\log(\omega)$ according to the formula

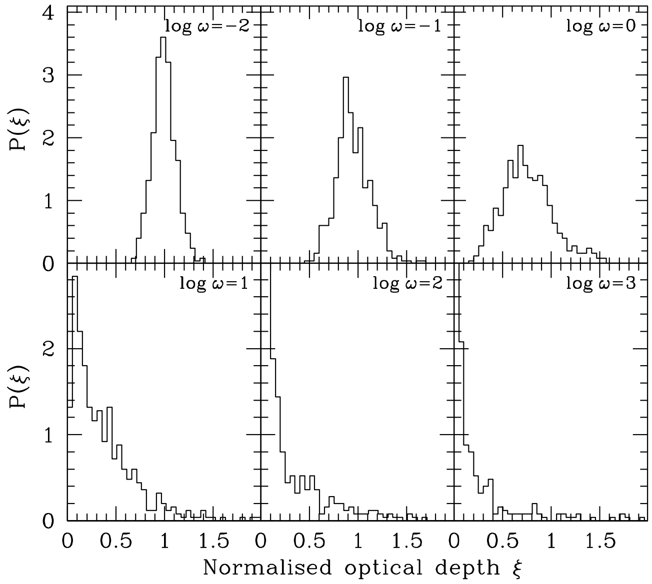

Fig. 5. Distribution of the normalised optical depth ξ under the influence of increasing ω values. The histograms represent the ξ distribution of 500 simulated spectra with $z_{\mathrm{QSO}} = 3$.

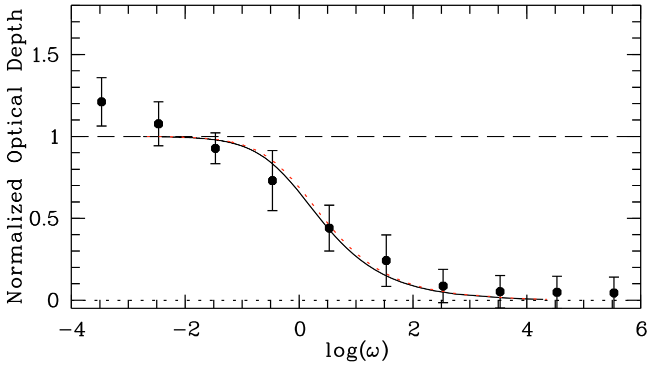

Fig. 6. Normalised effective optical depth versus ω for the combined sample of 40 quasars, binned in steps of $\Delta\log\omega = 1$. The curved lines are the best fit of the simple photoionisation model to the data, corresponding to a UV background of $\log(J_{\nu_0}) = -21.10$ (solid line) in units of $\mathrm{erg\,cm^{-2}\,s^{-1}\,Hz^{-1}\,sr^{-1}}$, while the dotted curve denotes to the fiducial UVB ($J^\star$) for the computation of ω. The horizontal dashed line illustrates the case of no proximity effect.

$$F(\omega) = \left(1 + \frac{\omega}{a}\right)^{1-\beta} \tag{7}$$

where a is the single free parameter which expresses the *observed* turnover of ξ and thereby provides the best-fit value of J_{ν_0}, since obviously $J_{\nu_0} = a \times J^\star$. The slope of the column density distribution was fixed to $\beta = 1.5$ (see Sect. 3 for details).

For the median redshift of our sample of $z = 2.73$ we thus obtain $J_{\nu_0} = (7.9 \pm 3.1) \times 10^{-22}\,\mathrm{erg\,cm^{-2}\,s^{-1}\,Hz^{-1}\,sr^{-1}}$, or in logarithmic units $\log J_{\nu_0} = -21.10^{+0.14}_{-0.22}$. This number is very close to the value of $\log J_{\nu_0} = -21.03$ reported by us in Paper I and is also consistent with several other literature estimates. A detailed comparison with the literature is hampered by the fact that the vast majority of previous UVB measurements were derived adopting the almost obsolete Einstein-de Sitter model. Typically, values for J_{ν_0} are then about a factor of 1.4 (0.15 dex) higher than in a Λ−Universe. Cooke et al. (1997) measured

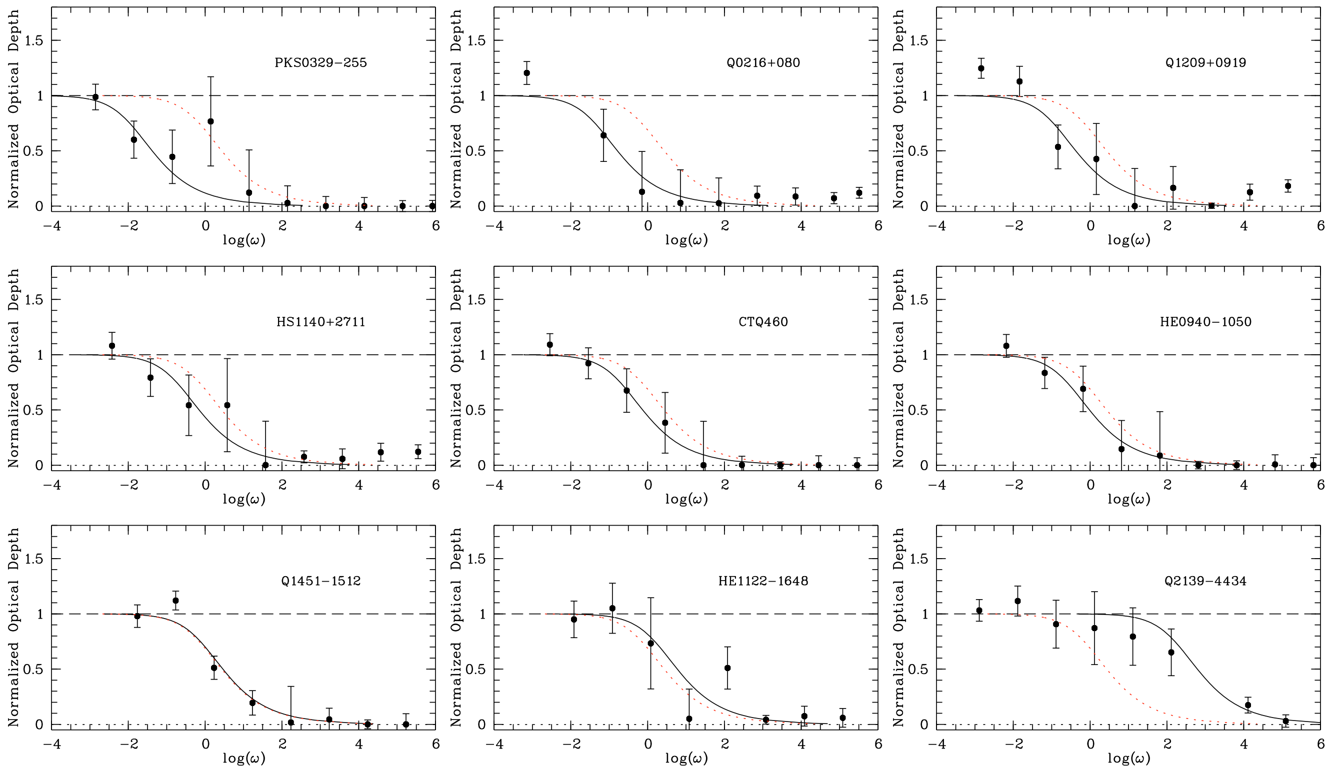

Fig. 7. The proximity effect signatures in individual lines of sight, for a subsample of 9 QSOs. Each panel shows the normalised effective optical depth ξ versus ω, binned in steps of $\Delta \log \omega = 1$, with the best-fit model of the combined analysis superimposed as the dotted red line (see Sect. 6). The solid lines delineate the best fit to each individual QSO as described in the text. This subsample was chosen for presentation purposes to show the variable strength of the proximity effect, going from *strong* (*top-left panel*) to *weak* (*bottom-right panel*).

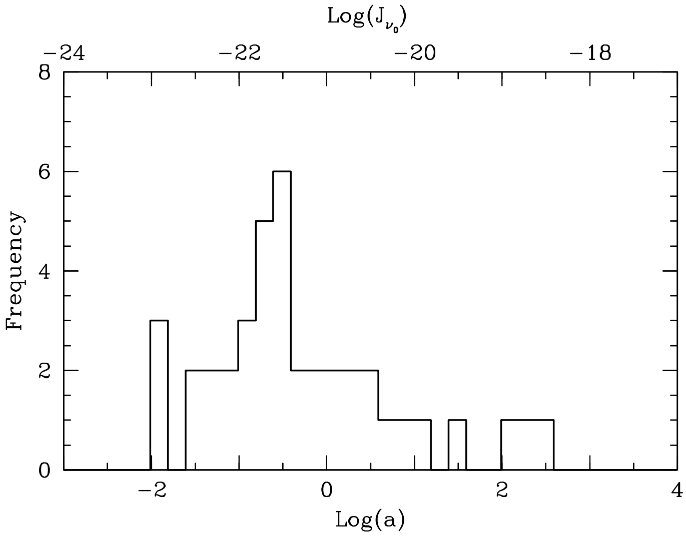

Fig. 8. Observed distribution of the proximity effect strength (given by $\log a$) for our sample of objects. The distribution is characterised by a prominent peak and a skewed profile which extends over several orders of magnitude in strength.

$\log J_{\nu_0} = -21.00^{+0.18}_{-0.15}$ on 11 high resolution quasar spectra using line statistics. Scott et al. (2000) obtained $\log J_{\nu_0} = -21.15^{+0.17}_{-0.43}$, applying the same method on more than a hundred spectra at ~1 Å resolution. Liske & Williger (2001) used the flux statistic on 10 QSO spectra with ~2 Å resolution and a *S/N* of ~40, obtaining $\log J_{\nu_0} = -21.45^{+0.30}_{-0.20}$.

While the formal errors of this measurement are small, there are reasons to believe that the proximity effect exploited this way delivers systematically too high values of J_{ν_0}. Overdense environments around quasars have been suggested as the prime reason; we shall demonstrate in the next section that in fact the averaging process inherent in the sample combination is responsible for a major bias in the UVB determination.

7. The proximity effect in individual lines of sight

7.1. The distribution of the proximity effect strengths

For our investigation of the proximity effect towards single lines of sight, the approach was essentially identical to that of the combined analysis: we computed the normalised effective optical depths for individual sight lines within a given range $\Delta \log \omega$ and checked whether ξ systematically decreases for high values of ω. For presentation purposes, the results of a subsample of 9 objects are displayed in Fig. 7, one panel per quasar (see Appendix A for the complete sample). The error bars are dominated by Poissonian shot noise, estimated from the simulations as described in Sect. 5.3. In each panel, $\xi(\omega)$ is shown for the fiducial reference value $J_{\nu_0} = J^{\star}$. Figures 7 and A.1 illustrate that in all cases, ξ decreases substantially as ω increases. Thus we conclude that the proximity effect is detected in all of our quasar spectra. This is in excellent agreement with our finding in Paper I, where in only 1 out of 17 low-resolution quasar spectra we failed to detect the proximity effect (and for that object, HE 2347−4342, we now detect a weak effect in the high-resolution UVES spectrum; see Appendix A).

We then applied the above fitting procedure (Eq. (7)) to each spectrum separately. The results are shown as the solid curves

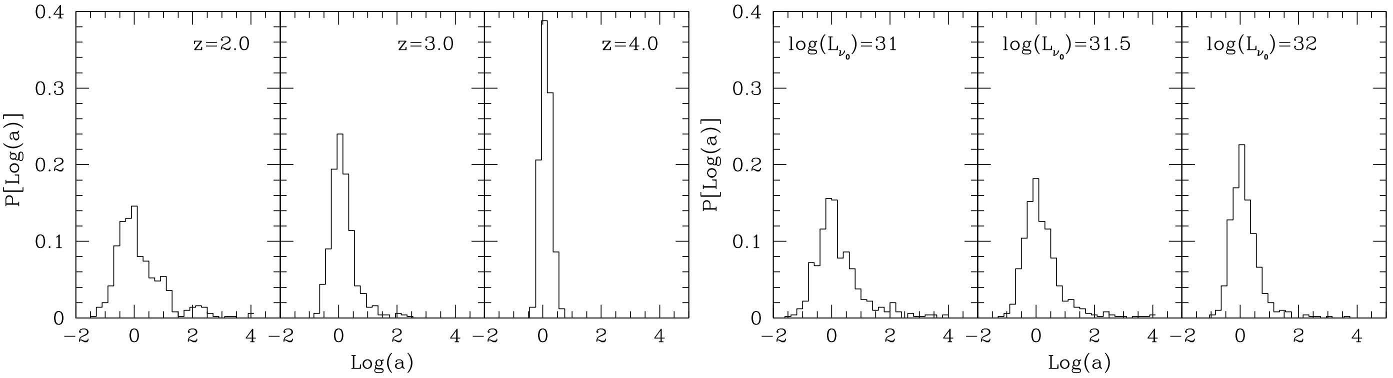

Fig. 9. Proximity effect strength distributions in our synthetic spectra for different quasar redshifts (*left-hand panel*) and luminosities (*right-hand panel*). The distributions are computed from 500 artificial sight lines generated by our Monte Carlo code as described in Sect. 3 and are affected only by Poissonian shot noise.

Table 3. The proximity effect strength $\log a$ along single lines of sight.

QSO	$z_{\rm em}$	$\log L_{\nu_0}^{\dagger}$	$\log a$
Q 1232+0815	2.575	30.91	-1.89 ± 0.37
Q 0329−385	2.438	31.48	-1.86 ± 0.29
PKS 0329−255	2.706	31.58	-1.86 ± 0.25
HE 0001−2340	2.278	31.68	-1.46 ± 0.36
HE 1347−2457	2.615	32.06	-1.43 ± 0.25
Q 0216+080	2.996	31.20	-1.26 ± 0.36
HE 2217−2818	2.414	32.02	-1.21 ± 0.31
Q 0109−3518	2.406	31.72	-1.10 ± 0.38
Q 1249−0159	3.668	31.27	-1.08 ± 0.22
PKS 2126−158	3.285	31.92	-0.99 ± 0.22
Q 1209+0919	3.291	31.42	-0.85 ± 0.29
Q 0913+0715	2.788	31.48	-0.84 ± 0.34
Q 0002−422	2.769	31.76	-0.78 ± 0.32
PKS 1448−232	2.222	31.50	-0.75 ± 0.47
Q 0055−2659	3.665	31.81	-0.67 ± 0.20
HS 1140+2711	2.628	31.94	-0.63 ± 0.35
HE 2243−6031	3.012	32.17	-0.61 ± 0.24
CTQ 0460	3.141	31.76	-0.61 ± 0.27
HE 0940−1050	3.089	32.13	-0.49 ± 0.26
Q 1621−0042	3.709	31.91	-0.49 ± 0.20
Q 1151+0651	2.758	31.21	-0.45 ± 0.46
PKS 2000−330	3.786	31.69	-0.45 ± 0.23
Q 0122−380	2.192	31.51	-0.42 ± 0.44
Q 1409+095	2.843	31.06	-0.33 ± 0.54
Q 0347−3819	3.229	31.66	-0.23 ± 0.30
Q 0420−388	3.120	31.93	-0.18 ± 0.32
Q 1451−1512	4.766	32.12	-0.01 ± 0.14
Q 1317−0507	3.719	31.35	$+0.13 \pm 0.31$
Q 0453−423	2.664	31.41	$+0.18 \pm 0.45$
HE 1122−1648	2.407	32.05	$+0.30 \pm 0.33$
HE 1158−1843	2.459	31.56	$+0.35 \pm 0.38$
BR 1202−0725	4.697	32.24	$+0.51 \pm 0.14$
Q 1223+1753	2.955	31.16	$+0.58 \pm 0.36$
CTQ 0247	3.025	31.66	$+0.76 \pm 0.25$
HE 2347−4342	2.886	32.05	$+0.87 \pm 0.17$
Q 2206−1958	2.567	31.57	$+1.15 \pm 0.21$
HE 1341−1020	2.137	31.17	$+1.51 \pm 0.14$
PKS 0237−233	2.224	31.93	$+2.07 \pm 0.12$
Q 2139−4434	3.207	31.39	$+2.32 \pm 0.26$
HE 0151−4326	2.787	31.92	$+2.57 \pm 0.15$

† Lyman limit luminosities and uncertainties $\left(\sigma_{\log L_{\nu_0}} \simeq^{+0.05}_{-0.1}\right)$ in units of erg s^{-1} Hz^{-1}.

in Fig. 7, while Table 3 summarises the fit results. The value of the fitting parameter a, which describes the horizontal offset of the solid curve relative to the dotted one, will be regarded in the following as a measure of the strength of the proximity effect signal. It shows significant scatter between the different quasars. Note that the zeropoint of $\log a$ is arbitrary and depends only on our assumed fiducial UVB value $J^{\star}$. Figure 8 presents the measured proximity effect strength distribution (PESD), i.e. the distribution of $\log a$ for our sample.

Three major characteristics emerge:

(i) the distribution covers almost five orders of magnitude in a, ranging from a very weak proximity effect ($a \gg 1$) to a very strong one ($a \ll 1$);
(ii) it shows a well-defined peak; and
(iii) it is significantly skewed. In the following we will investigate the effects behind these properties.

7.2. The effects of variance between sight lines

The most obvious contributor to a spread in proximity effect strengths is the variance in the absorber distribution between different lines of sight. To investigate this effect we employed our Monte Carlo simulated spectra, for which by design this variance can be accurately described as a pure Poissonian process.

The proximity effect was introduced in the synthetic spectra as a reduction in the optical depth by a factor $1 + \omega$, with ω given by Eq. (3). We first fixed the luminosity of the quasar to a value of $\log(L_{\nu_0}/\mathrm{erg\,s^{-1}\,Hz^{-1}}) = 31.5$ and considered three different redshifts: $z = 2.0$, 3.0, and 4.0, in order to see how the distribution of a changes with z. Then we took a constant redshift of $z = 3.0$ and considered three quasar luminosities: $\log(L_{\nu_0}/\mathrm{erg\,s^{-1}\,Hz^{-1}}) = 31$, 31.5, and 32. The UV background was fixed to $J_{\nu_0} = J^{\star}$ in both cases. Our results are presented in Fig. 9; recall that high a values imply a weak proximity effect.

Two main characteristics become apparent in Fig. 9: the distributions are significantly skewed, and the skewness decreases towards higher redshifts and higher luminosities. This asymmetry is a direct result of the non-linear dependence of ω on redshift as expressed in Eq. (3). Towards the quasar redshift equal $\Delta \log \omega$ bins correspond to progressively smaller Δz intervals. Very close to the QSO, the (Poissonian) distribution of the number of absorbers per $\Delta \log \omega$ bin deviates significantly from a Gaussian. Similarly the distribution of effective optical depth becomes skewed at $z \to z_{\rm em}$, resulting in high $\tau_{\rm eff}$ values being more likely than expected for a normal distribution. The asymmetry of the PESD directly reflects this statistical effect.

The dependence with redshift can be explained by the fact that on the one hand, Poisson noise has a weaker impact at high redshifts and on the other hand, an increasing luminosity is capable of a substantial reduction in the optical depth further away from the quasar emission, overionising even strong systems in the quasar vicinity.

Because of the asymmetric nature of the PESD at any given redshift and luminosity, one tends to overestimate the best fit values of Eq. (7) when combining multiple sight lines together in an averaging process. By comparing how the distribution widths evolve with redshift and luminosity, we conclude that luminosity has a weaker effect than redshift in changing the shape of the PESD.

A remarkable feature of Fig. 9 is the fact that the mode of the distribution always stays at the input value corresponding to $\log a = 0$. We exploit this property in the next section.

7.3. An unbiased measurement of the UV background

Unfortunately, we do not have 500 observed quasar spectra at one particular redshift or luminosity, but rather a quasar sample distributed in redshift and luminosity. We created another set of simulated spectra to predict the "PESD as observed", assuming that only Poissonian variance contributes to the spread of $\log a$, in the following way: we constructed 40 simulated QSO spectra with the condition that their redshifts and luminosities were exactly the same as the observed ones, and we constructed the PESD for this "sample". We repeated the process 500 times and averaged the PESD. The result is shown in Fig. 10 as a thin histogram, superimposed on the observed data of our quasar sample.

The predicted distribution of the proximity effect strength parameter $\log a$ looks amazingly similar to the observed one. In particular, the degree of asymmetry is very nearly the same. The observed PESD seems to show a slightly narrower core, and it certainly has some outliers on both sides, at $\log a \simeq -2$ and $\log a > 2$. We interpret this excellent agreement as an indication that the statistical fluctuations of the distribution of absorption features between individual sight lines is responsible for most of the spread and in fact for most of the asymmetry in the PESD.

What does this imply for the UV background? We again find that the modal value of the "as observed" distribution recovers the input UVB intensity, whereas the combined analysis heavily overestimates it. From the 500 realisations we derive that the mode of the PESD of 40 quasars is consistent with the value of input model to within ±0.15 dex. Similarly we can quantify the bias introduced by the combined analysis. For this purpose, we computed the best-fit $\log\, a$ as in Sect. 6 and averaged it over the 500 realisations. Typically, the averaged value of J_{ν_0} is overestimated by $\Delta \log a = 0.3$ dex, or a factor of 2.

From Fig. 10 we estimated the position of the mode of the observed PESD to be located at $\log a = -0.51$ and converted it into a measurement of the UVB, yielding a value of $\log J_{\nu_0} = -21.51 \pm 0.15$. The uncertainty was derived from the dispersion of the mode in the simulated PESDs. This value of the UVB is 0.4 dex lower than the best-fit of the combined proximity effect analysis given in Sect. 6.

For completeness we also considered what happens when one computes the average of the best-fit $\log a$ values for individual quasars (as listed in Table 3), instead of fitting the average $\xi - \omega$ profile. This results in a UVB value of $\log J_{\nu_0} = -21.24 \pm 0.17$, lower than the outcome of the combined proximity effect analysis as well, but still much higher than the modal value (and also systematically offset in the simulations).

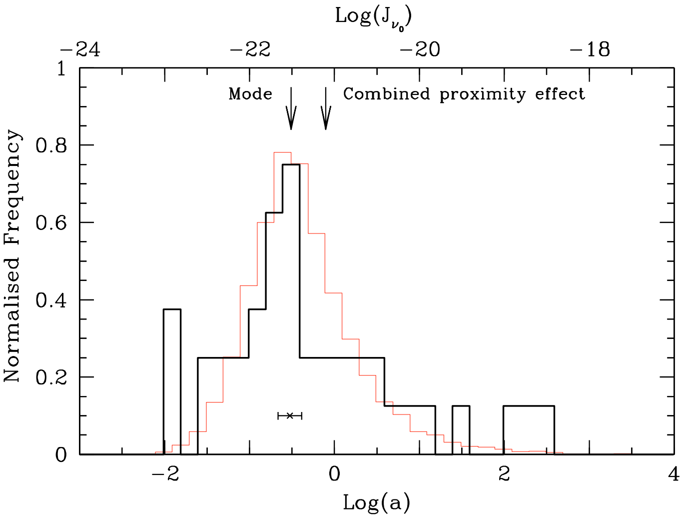

Fig. 10. Comparison between observed (thick) and simulated (thin) distribution of the proximity effect strength (given by log(a)) for our sample of quasars. We mark the position of the mode of the observed distribution and the relative error associated to it. The error bars are computed from the dispersion of the mode in the 500 realisations of the simulated sample. We also display the value of the UVB computed in the combined analysis of the proximity effect.

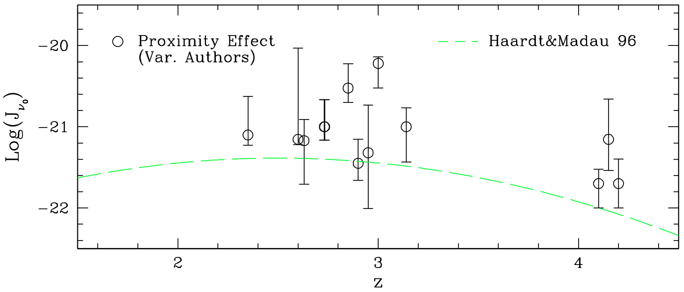

Fig. 11. Redshift evolution of the UVB modelled by Haardt & Madau (1996) in comparison to previous measurements of the UVB via the proximity effect (Bajtlik et al. 1988; Lu et al. 1991; Giallongo et al. 1993; Williger et al. 1994; Bechtold 1994; Fernández-Soto et al. 1995; Srianand & Khare 1996; Giallongo et al. 1996; Lu et al. 1996; Savaglio et al. 1997; Cooke et al. 1997; Scott et al. 2000; Liske & Williger 2001), all for an Einstein-de Sitter universe.

We compiled several literature results in measuring the UVB by the proximity effect together with our new our results in Figs. 11 and 12. As said above, the cosmological model employed does have an effect on the UVB result. Figure 11 collects literature measurements that were performed for an Einstein-de Sitter model. Most of them agree poorly with the UVB model by (Haardt & Madau 1996, which was computed for the same cosmological model), in the sense that the measurements are systematically higher.

Figure 12 puts our new determination of J_{ν_0} into context. It is remarkable that our modal value is almost exactly on the predicted curve based on the newer UVB model by Haardt & Madau (2001). Their computation was based on assuming a combined contribution of QSOs and star-forming galaxies to the UV background, now performed for a Λ universe. It is also fully consistent with the determination of the UVB photoionisation rate by Bolton et al. (2005) obtained by matching the observed Ly forest transmission to cosmological simulations. It is equally evident that our "combined value" is too high, as is our similarly obtained best-fit value in Paper I.

We summarise this section by stating that the distribution of proximity effect strengths as determined in individual quasar spectra is largely consistent with a purely Poissonian random

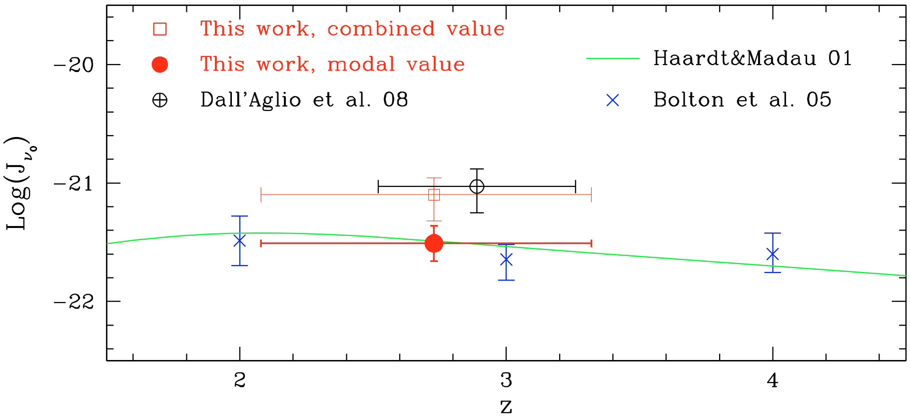

Fig. 12. Measured intensity of the UVB for a Λ universe. Our best estimate is the modal value of J_{ν_0} (filled red circle); the biased "combined value" (open square) as well as the similarly obtained value from Paper I (open circle) are shown for comparison. Also shown are the most recent evolving UVB model by Haardt & Madau (2001) (continuous green line) and the determination by Bolton et al. (2005). The horizontal bars indicate the lower and upper quartile of the quasar redshifts.

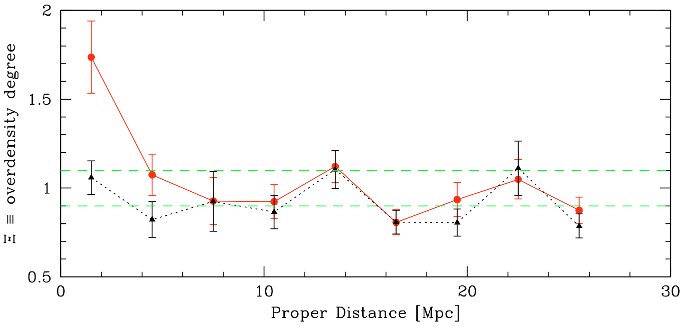

Fig. 13. Average overdensity degree Ξ as function of proper distance for the complete sample of quasars (solid line) and in a subsample with Ξ consistent with no sign of overdensities within 3 Mpc from the quasar (dotted line). The two horizontal lines mark the $\pm 1\sigma$ scatter expected from our simulation in the case of no overdense environment.

process. We thus understand why the PESD is asymmetric, and why previous measurements based on averaging sample properties were bound to overestimate the UVB background. So far we have identified the modal value of the PESD as a largely unbiased estimator of the UVB. In the next section we will improve on this estimator by proposing a hybrid approach that also takes physical overdensities into account.

8. The role of overdensities around quasars

8.1. Quantifying overdensities

We have demonstrated above that much of the disagreement between proximity effect and other measurements of the UVB is due to the asymmetric shape of the PESD, even for the idealised case of purely Poissonian variance between sight lines. However, this does not imply that other effects can be neglected altogether. The most suspicious additional bias in this context is the degree of typical H^0 overdensity within a few Mpc around quasars. Obviously, if a quasar environment is overdense and thus more likely to show high column density absorption than the general Lyman forest, the proximity effect will appear to be weakened (Loeb & Eisenstein 1995).

This issue has been recently addressed by Rollinde et al. (2005) and Guimarães et al. (2007) using both observations and numerical simulations. Their basic approach consisted of a comparison of the cumulative optical depth probability distributions at difference distances to their quasars. Close to the quasars, that distribution deviates from the one for the general Lyman forest. Assuming that the UVB photoionisation rate is well constrained from the cosmic mean H^0 opacity and accounting for the expected proximity effect signature based on the known quasar luminosities, they concluded from the discrepancy between the measured and predicted distributions that quasars reside in physical overdensities of a factor of a few (averaged over $\sim 2.5\,h^{-1}$ proper Mpc). The amount of inferred overdensity depends, as one would expect, on the adopted value of the general UVB photoionisation rate.

Here we approach the same problem from a different angle. We also assume that the mean UVB photoionisation rate, or the mean intensity J_{ν_0}, can be measured. We adopt the modal value of the PESD estimated in Sect. 7.3, which we demonstrated above to be in excellent agreement with other methods of estimating the UVB. We then again consider each individual quasar in our sample in turn, aiming at measuring the *distribution* of (over)density properties. For the present paper we are not interested in estimating physical overdensities, but only in identifying the quasars with strongly overdense environments. We therefore adopted a pragmatic definition of "density" that simply involves the absorber optical depth within a certain filter length as a proxy. We computed this "overdensity degree" Ξ in the following way:

1. We reconstructed the optical depth profile $\tau^*(z)$, *removing the radiative influence of the quasar* by multiplying the optical depth $\tau(z)$ in the Lyα forest by $1 + \omega(z)$. For the UVB intensity we used the modal value of the PESD, $\log J_{\nu_0} = -21.51$. Despite the high *S/N* of our spectra, this procedure required particular attention for transmission points falling below zero and above unity due to noise and continuum uncertainties. The negative points belong to saturated lines which will become even more saturated after the inverse correction for the proximity effect; such points were left uncorrected. Pixels with transmission values $T > 1$ were also disregarded in the correction in order to prevent numerical problems or an artificially increased *S/N* level. Both cases apply only to a small number of pixels, and their in- or exclusion does not affect the results.
2. From the corrected $\tau^*(z)$ we computed the effective optical depth in bins along the line of sight and divided it by the expected values at the appropriate values of z (given by Eq. (1)). This procedure had to be carried out for each object separately. We define this ratio of effective optical depths as the *overdensity degree* Ξ. We performed this calculation for different bin sizes, corresponding to increments of 2, 3, 5 and 8 proper Mpc. Qualitatively, the results are the same, with a bin size of 3 Mpc showing the clearest trends. We only quote results for that bin size in the following.

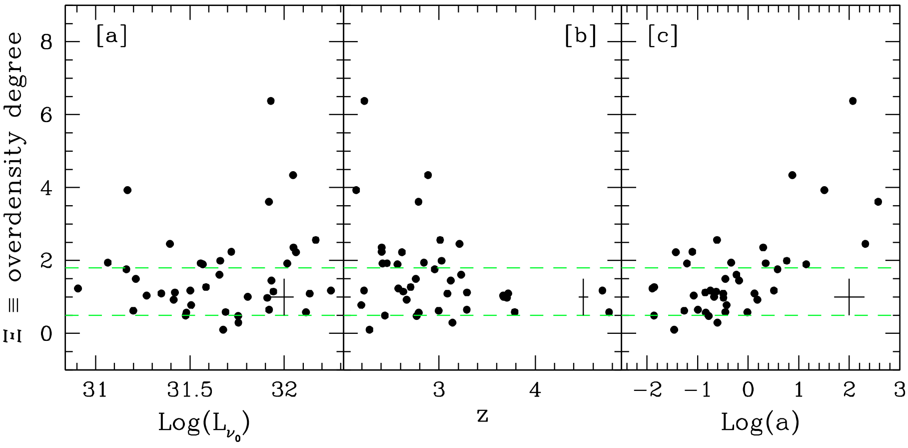

Fig. 14. Dependence of the overdensity degree on quasar luminosity (panel **a**)), redshift (panel **b**)), and on the proximity effect strength (panel **c**)). The uncertainties relative to each measurements are represented by the solid cross in the respective panel. The solid line in *the right-hand panels* shows the least-square linear fit to the data. In each panel the dashed horizontal lines give an estimate of the amount of Poissonian shot noise in the simulations of the forest for $R_0 = 3$ Mpc from the emission redshift, as $\pm 1\sigma$ envelopes around the expected $\tau_{\rm eff}$ in the case of no overdensity ($\Xi = 1$).

3. We then merged all lines of sight, resulting in 40 estimates of Ξ per distance bin. In each bin we estimated the mean and the standard deviation of Ξ. We used our Monte-Carlo simulated spectra to reproduce our QSO sample and thereby estimated the amount of variance in Ξ attributed to pure Poisson noise.

8.2. Overdensity distribution

The dependence of the average Ξ as a function of distance is presented in Fig. 13 (solid line). At large distances (>5 Mpc), Ξ fluctuates around unity as predicted by perfect Poissonian noise. Only in the innermost bin for ≲3 Mpc does the mean value of Ξ increase towards an overdensity degree of a factor of 2 (in units of optical depth). So far this can be seen as supporting the notion of quasars *typically* residing in overdense regions (e.g. D'Odorico et al. 2008). However, in the same panel we also show the average Ξ if the 10 objects (25% of the sample) with the highest individual overdensities are removed (see below for details of this deselection). For all bins beyond ∼5 Mpc, the run of Ξ with distance is statistically indistinguishable for the two samples. Only for the nearest two bins the two profiles deviate, in the sense that the dotted profile (based on 75% of the sample) is fully consistent with no overdensities at all.

Figure 14 shows the individually measured "overdensity degrees" within the innermost 3 Mpc bin as a function of quasar luminosity at the Lyman limit, quasar redshift, and proximity effect strength $\log a$ (cf. Sect. 7.1), respectively. This diagram reveals that the corrected effective optical depths for individual quasars range from close to zero to up to 6 times larger than in the mean Lyα forest. The horizontal dashed lines again indicate the amount of scatter ($\pm 1\sigma$) expected for pure Poissonian variance within the same physical scale around each of the QSOs.

Panel a shows that there is no systematic tendency of Ξ to vary with the quasar Lyman limit luminosity. The spread appears to be somewhat larger at high luminosities, which may reflect the expected trend of luminous quasars to reside in more massive environments. But there are also several high-L objects with Ξ values around unity.

Regarding the redshift dependence depicted in Panel b of Fig. 14, no significant trend can be seen here either. There may be a deficit of high overdensities for $z > 3$, but this could equally be an effect of small number statistics.

However, panel c of Fig. 14 reveals some dependence between Ξ and proximity effect strength $\log(a)$. The four QSOs with $\Xi > 3$ are among the six objects with the weakest proximity effect (highest values of $\log a$). A quantitative test using the standard linear correlation coefficient r shows that $\log \Xi$ is indeed correlated with $\log a$, $r = 0.6$ (with a probability of <1% of no correlation), but that this trend is strongly driven by the few points with $\Xi > 3$. Without these points, the correlation coefficient reduces to $r = 0.4$, and there is a 3% probability of no intrinsic correlation.

8.3. Effects of overdensities on the proximity effect strength distribution

We now investigate how the presence of some fraction of the QSOs residing in dense environments changes the properties of the PESD. We generated a new sample of synthetic spectra at $z = 2$, 3 and 4, respectively, at a fixed luminosity of $\log(L_{\nu_0}/\text{erg s}^{-1}\,\text{Hz}^{-1}) = 31.5$, with the difference that we now required that our sight lines show excess absorption near the emission redshift. We did not assume any particular radial distribution for the overdensity profile, but simply continued to populate the spectrum within 3 Mpc with lines until the effective optical depth reached a given threshold. We constructed two samples, for overdensities of $\Xi = 2$ and 4, respectively, to approximately mimic our observational results (500 spectra for every Ξ).

These simulations show that if all quasars had the same enhanced expectation value $\langle\Xi\rangle$, the *shape* of the PESD would not be greatly affected for all studied redshifts. The main effect would be a global shift of the PESD towards higher $\log a$ values, with the shift increasing as $\langle\Xi\rangle$ becomes larger. This is shown in the top panel of Fig. 15, where we plotted the PESD for three expectation values of $\langle\Xi\rangle = 1$, 2, and 4, respectively. Already for an average enhancement of $\langle\Xi\rangle = 2$, the peak of the PESD is shifted by ∼0.6 dex.

It follows that if quasar environments are systematically overdense by some uniform factor, we would be unable to tell this from our data alone: our empirical determination of Ξ depends on assuming the correct global J_{ν_0}. If the mode of the PESD is biased by some factor, we would *underestimate* the Ξ values of the individual quasars by the same factor, effectively renormalising the *observed* Ξ scale to an expectation value of unity. Of course, this is nothing but yet another manifestation of the well-known degeneracy between the UVB and overdensities around quasars.

However, such a simple picture of all quasars having the same density enhancement factor would be highly unrealistic. If quasars reside in overdensities, the enhancement will have a distribution stretching over at least a factor of few. Because the shift of the PESD depends on $\langle\Xi\rangle$, this will lead to a broadening of the PESD by an amount depending on the physical

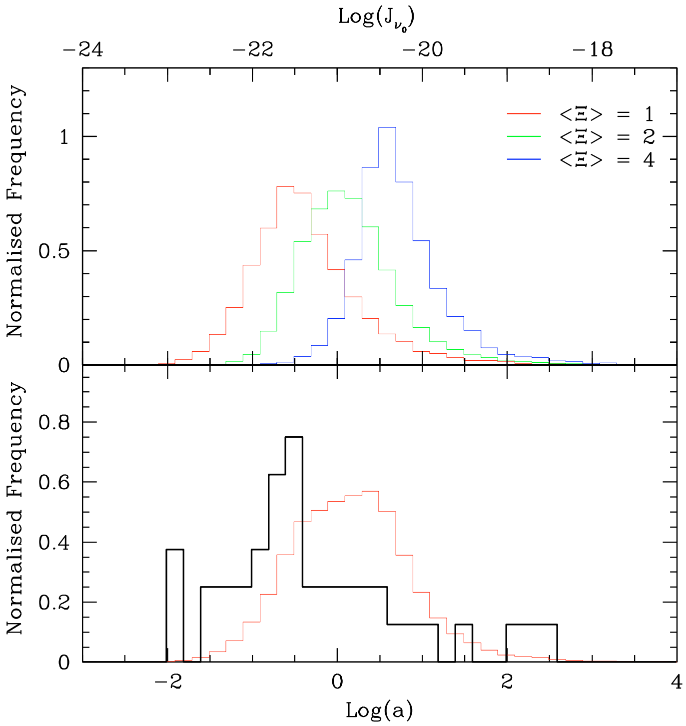

Fig. 15. *Top panel*: expected PESD computed from Monte-Carlo simulations for different expectation values of the overdensity degree (Ξ = 1, 2, 4, respectively). The main effect is a substantial shift towards an on average weaker proximity effect. *Bottom panel*: comparison of the observed PESD and the expectation for an assumed Gaussian distribution of overdensities (see text for details).

spread of overdensities. Notice that this spread will come on top of the inevitable scatter due to Poissonian variance. As an example toy model, we show in the bottom panel of Fig. 15 the modified PESD for an assumed physical rms scatter in $\langle \Xi \rangle$ of 0.25 dex. The predicted distribution is considerably different; it is much broader and more box-shaped, and certainly much less in agreement with the observed PESD than the one for $\langle \Xi \rangle = 1$. While the assumption of a scatter of 0.25 dex is entirely ad-hoc, the example shows that the PESD reacts quite sensitively, and a very small physical dispersion around the expectation value of Ξ is required to make observed and predicted PESD consistent. This is naturally obtained only if the expectation value for most quasars is close to $\langle \Xi \rangle \approx 1$.

These considerations strongly support the notion that there is no strong *systematic* overdensity bias for the proximity effect. While the excellent agreement between our modal estimate and other ways of determining the UVB intensity (Fig. 12) is already highly suggestive, we cannot of course use this agreement both to justify our method *and* regard it as an indepenent measurement of the UVB. The comparison of expected and observed PESD shapes adds independent information from the distribution properties and breaks the UVB-overdensity degeneracy.

Clearly some fraction of objects sits in overdense regions. This, however, only produces a tail to the PESD by adding some high values of log a. A comparison of Figs. 14c with 10 shows that the objects with strong overdensities are exactly those lying outside the prediction for the simple Poissonian model.

We note in passing that there is no reason to interpret the few quasars showing an extremely strong proximity effect as sitting in "underdensities". The three objects with the lowest log a values have a mean Ξ very close to unity (see Fig. 14c), and only one object is located outside of the $\pm 2\sigma$ envelope of Ξ expected for pure Poissonian fluctuations around the mean density.

8.4. A hybrid method of estimating the UV background

In the following we adopt the notion that only a relatively small fraction of at most ~25% of our quasars is affected by significant overdensities. If this is true, then for a completely unbiased estimation of the UVB we need to:

(i) remove the quasars with biased environments;
(ii) correct for the asymmetry bias in the proximity effect strength distribution.

In order to conduct the first step we had to identify outliers in the Ξ distribution. However, recall that Ξ is based on the assumption that we already know the UVB background. As an initial guess we adopted the modal value from the PESD, from which we then could compute Ξ for all quasars. There is no obvious cutoff, and many quasars have Ξ values that are consistent with weak overdensities. We decided to make a conservative cut in the sense that we would rather avoid too many even mildly overdense objects. We set the threshold at $+1\sigma$ (predicted scatter for Poissonian variance), implying that quasars with $\Xi > \Xi_0 = 1.8$ would be excluded from the analysis. This was the case for 10 objects, or 25% of the sample.

We then constructed the PESD based on the remaining 30 objects. The modal value remains unchanged, but the uncertainty obviously increases (0.2 rather than 0.15 dex). The fact that the mode of the PESD is robust against the inclusion or exclusion of 25% of the sample is certainly encouraging. It is also clear that it would not be possible to use a much smaller fraction of objects, as the uncertainties of estimating the mode would rapidly go up.

Next, we determined the systematic offset of the "combined sample averaging" estimator (used in Sect. 6) due to the asymmetry of the PESD. We proceeded as follows: we generated mock quasar samples from the Monte Carlo simulated spectra, assuming no systematic overdensity bias, with the same redshift and luminosity distributions as the observed sample. We removed those objects showing apparent overdensities (occurring because of statistical noise) and determined the best-fit UVB value using the standard sample combination method as described in Sect. 6. Repeating this step 500 times, we averaged over the differences to the input UVB, obtaining a mean offset of $\Delta \log a = 0.27$ dex.

Finally, we conducted the same procedure for the observed sample with $\Xi < 1.8$, performing a least-squares fit of Eq. (7) to the data and correcting the resulting value by the above offset. The inferred value is $\log J_{\nu_0} = -21.46^{+0.14}_{-0.21}$, which we consider as the best and most robust estimate of the global UV background intensity for our sample.

In order to find out how much the method depends on the adopted criterion to eliminiate outliers, we repeated the described procedure once more, but now setting the threshold at $+2\sigma$, corresponding to $\Xi_0 = 3.1$. This implies that only the four objects with the highest Ξ values were excluded from our sample. We redetermined the mean offset, which remained unchanged. The least-squares fit of Eq. (7) to the data, corrected for the relative offset, yields again a value of $\log J_{\nu_0} = -21.49^{+0.14}_{-0.21}$, demonstrating that our hybrid method is highly robust and quite insensitive to the outlier criterion.

Determining the UVB intensity using this hybrid method has one important advantage over the modal PESD estimator: it depends less critically on the sample size. The mode is a robust

Table 4. Summary of our UV background measurements and employed methods, for the sample median redshift $z = 2.73^{\dagger}$.

Method	$\log J_{\nu_0}$
Fit to combined sample	$-21.10^{+0.14}_{-0.22}$
Mode of PESD	$\mathbf{-21.51 \pm 0.15}$
Mean of individual $\log a$	-21.24 ± 0.17
Fit to combined subsample ($\Xi < 1.8$)	$-21.19^{+0.14}_{-0.21}$
Fit to combined subsample ($\Xi < 1.8$,corrected)	$\mathbf{-21.46^{+0.14}_{-0.21}}$

† The two boldfaced rows represent the unbiased estimates.

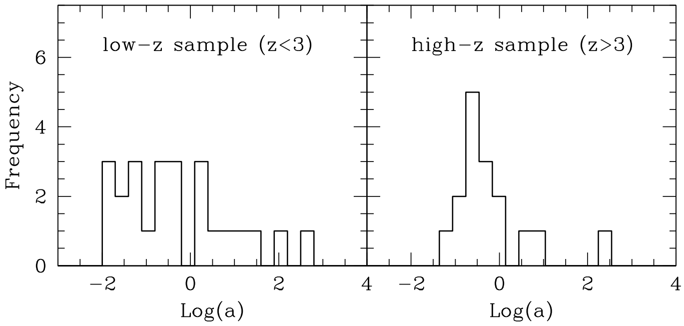

Fig. 16. Observed PESD for our sample of quasars divided into two redshift intervals. The shapes of the two PESDs differ substantially from each other as predicted in Sect. 7.2.

statistical quantity only if the histogram from which it is estimated is reasonably well defined. In the next section we will split the sample into subsets to investigate the redshift evolution of the UVB. It will be seen that the PESD of such subsamples can become rather broad, inhibiting any confident mode estimation. The hybrid technique, on the other hand, involves straightforward averaging and therefore also works for smaller samples.

Table 4 summarises all our different methods of estimating the UVB intensity and the resulting values.

9. The redshift evolution of the UV background

The high *S/N* of our data and the size and redshift range of the sample prompted us to explore whether we could split the sample into subsets of different redshifts and still get meaningful constraints on the UVB.

As a first attempt we divided the sample into two subsets with $z < 3$ and $z > 3$. For each subset we constructed the PESD separately, shown in Fig. 16. The distributions look substantially different from each other. The PESD of the lower redshift subset is very broad, and no clear peak can be recognised. On the other hand, the high redshift PESD is significantly narrower and displays a well-defined maximum. The overall behaviour is qualitatively consistent with the predictions of Fig. 9 based on our Monte Carlo simulations, where we found that the widths of the PESD should decrease as redshift increases (Sect. 7.2). The modal value obtained from the high redshift sample is $\log J_{\nu_0} \simeq -21.6$, slightly lower than the overall best estimate. In the lower redshift subset, even a rough guess of the distribution mode is impossible.

A more powerful way of estimating the UVB intensity is the hybrid method described in the previous subsection. We now employed this method to investigate the redshift evolution of the UVB. After merging all quasar spectra in the same way as for measuring the evolution of the Lyα effective optical depth (Sect. 4) we sampled the Lyα forest in redshift bins of $\Delta z = 0.2$. We used only the forest in the redshift range $2 \lesssim z \lesssim 4$ in order not to be affected by small number statistics. For every bin we fitted Eq. (7) to the data and obtained a preliminary estimate of J_{ν_0}. These values are still systematically high, both as a result of the PESD asymmetry and because of the influence of overdense lines of sight. In particular, the redshift ranges at $z \sim 2.2$ and at $z \sim 2.9$ are heavily affected by the latter effect, as at these redshifts we find the majority of objects with a strongly overdense environment (cf. Fig. 14). In such narrow redshift bins, the values of the UVB are extremely sensitive to locally enhanced absorption, causing deviations of up to 1.3 dex.

Table 5. UV background intensity as function of redshift for the set of quasars that show overdensity degree $\Xi \leq 1.8$ as plotted in Fig. 17.

$< z >$	$\log J_{\nu_0}$	$\sigma_{\log J_{\nu_0}}$
2.10	−21.15	0.20
2.30	−21.89	0.20
2.50	−21.20	0.19
2.70	−21.62	0.19
2.90	−21.46	0.20
3.10	−21.50	0.20
3.30	−21.91	0.20
3.55	−21.61	0.20
3.80	−21.71	0.21

We now followed the same recipe as in Sect. 8.4 above: we removed from the sample those objects with $\Xi > 1.8$ within the innermost 3 Mpc. We then applied the combined average estimator for each redshift interval and applied the PESD asymmetry bias determined from the simulations. We obtained in total eight values of J_{ν_0}, for eight different redshift bins as listed in Table 5. These result are presented as black points in Fig. 17, where the horizontal bars indicate the redshift interval and the vertical bars are the statistical errors.

The top panel of Fig. 17 shows that our measurements do suggest a certain evolution of the UVB intensity with redshift. Fitting a simple least-squares linear relation to the data points we get

$$\log J_{\nu_0}(z) = (-0.20 \pm 0.14)\, z + (-21.0 \pm 0.4). \tag{8}$$

This fit (depicted as the solid line in the top panel of Fig. 17) yields residuals fully consistent with random errors. However, the slope is not very steep, and in view of the size of the error bars it is appropriate to ask whether evolution is actually *demanded* by the data. For comparison we considered also the null hypothesis of no evolution, which is represented by the horizontal dashed line in Fig. 17). The quality of that model is somewhat poorer, but a KS test gives still 10% acceptance probability, which is at best a marginal rejection. We can therefore only tentatively claim to detect the UVB evolution within this redshift interval. In a different take, we can confidently exclude a very steep redshift evolution, such as would be predicted from a UV background made predominantly of quasar light.

How do these results compare with other works aimed at estimating or predicting the UVB evolution at similar redshifts? We first consider the prediction by Haardt & Madau (2001). They constrained $J_{\nu_0}(z)$ by integrating the contributions of the observed quasar and young star-forming galaxy populations, accounting also for intergalactic absorption and re-emission. Their predicted redshift evolution of the UVB intensity is depicted as the solid green line in the lower panel of Fig. 17). The agreement with our data points could hardly be better; in particular,

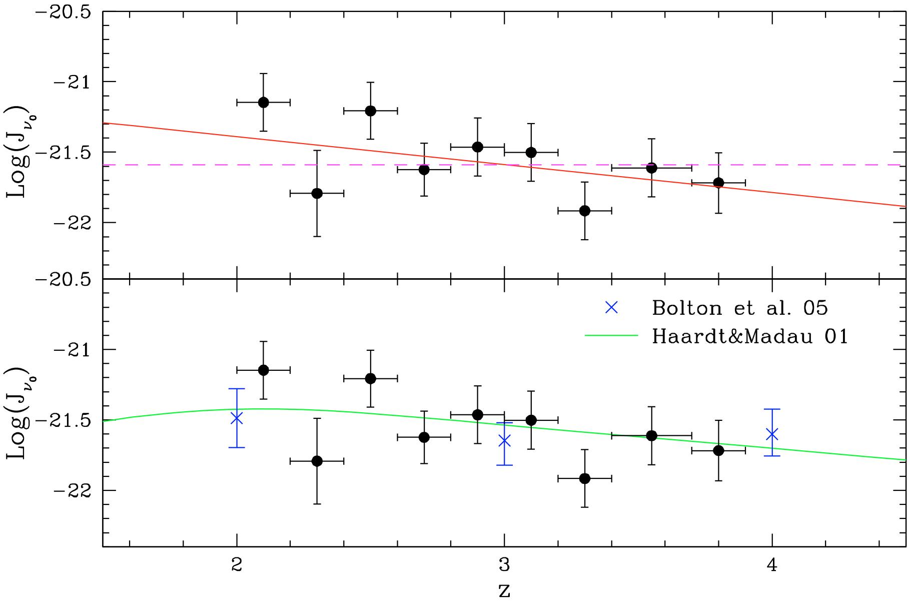

Fig. 17. Evolution of the mean intensity of the UV background with redshift from those quasars with overdensity degree $\Xi < 1.8$ (see text for details). We estimated the UVB using the combined analysis of the proximity effect in $\Delta z = 0.2$ intervals over the range $2 \lesssim z \lesssim 4$. *Top panel*: $\log J_{\nu_0}(z)$ in comparison to a constant evolutionary model (dashed) and a linear fit to the data (solid). *Bottom panel*: $\log J_{\nu_0}(z)$ in comparison to the model by Haardt & Madau (2001) and the more recent determination of the UVB evolution from Bolton et al. (2005). The errors in the z direction represent the range used to measure the average UVB.

the shallow slope is almost exactly reproduced. We roughly estimate a slope of $\mathrm{d}J/\mathrm{d}z = -0.16$ for the Haardt & Madau model at $z \gtrsim 2.2$, which is extremely close to our best-fit value of −0.2. Nevertheless it should be emphasised that the galaxy contribution to the UVB crucially depends on the poorly constrained escape fraction of Lyman continuum photons from galaxies (e.g. Shapley et al. 2006; Gnedin et al. 2007).

Recently, several studies calibrated the outcome of hydrodynamical IGM simulations through the measured Lyα forest opacity to estimate the photoionisation history of intergalactic hydrogen (e.g., Bolton et al. 2005; Faucher-Giguère et al. 2008a). These studies typically gave an approximately constant UVB intensity within the range $2 < z < 4$. As an example we show the results of Bolton et al. (2005) by the crosses in the lower panel of Fig. 17). As stated above, a no-evolution scenario as found by these studies is also consistent with the errors, and our results are also consistent with those of Bolton et al. (2005) and Faucher-Giguère et al. (2008a).

At any rate, our measurements confirm the prevailing assumption that quasars alone are unable to keep the IGM at a highly ionised state at redshifts larger than three. The integrated UV emissivity of AGN has a maximum very close to $z = 2$ and drops by about an order of magnitude towards $z = 4$ (Wolf et al. 2003; Hopkins et al. 2007), whereas we find the UVB intensity to fall by only ~0.2 dex (2σ limit is 0.48 dex). This strengthens the notion for a non-negligible contribution by star-forming galaxies to the UV background radiation field; their fractional contribution increases when going to higher redshifts.

We can make a simple back-of-an-envelope estimate of the mixing ratio between quasars and stars by assuming that the absolute UV emissivity of star-forming galaxies is roughly constant with redshift between $z = 2$ and $z = 4$. Since the integrated quasar emissivity at $z = 4$ falls to ~10% of its $z = 2$ value (Hopkins et al. 2007), and using our best-fit measurement of the overall UV background evolution (adopting a factor 0.4 between $z = 2$ and $z = 4$), we obtain that the H^0 photoionisation rate at $z = 2$ is dominated by quasars by a factor of ~2 over star forming galaxies. At $z = 4$, galaxies would then dominate by a factor of 5 over quasars. Any change towards making the total UVB evolution more constant with redshift would increase the fraction of starlight in the UVB.

10. Conclusions

We have analysed the largest sample of high-resolution quasar spectra presented in a single study to date. We demonstrated that the line-of-sight proximity effect is a universal phenomenon that can be found in the spectrum of essentially every individual high-redshift quasar. While in Paper I we arrived at the same conclusion using low-resolution spectra, we now can significantly reinforce this claim. In particular, continuum placing uncertainties, which were a bit of an issue in Paper I, play absolutely no role now, given the high spectral resolution and high *S/N* data exploited in this paper.

Our study rehabilitates the proximity effect as a tool to investigate the intensity at 1 Ryd (more accurately: the H^0 photoionisation rate) of the cosmic ultraviolet background. Previous investigations using the proximity effect nearly always produced UVB estimates that were suspiciously high and indeed at variance with other means to estimate or predict the UVB. It has been suggested in the literature that quasars typically reside in denser than average large-scale environments, and that therefore excess absorption biases the proximity effect to appear too weak, resulting in an overestimated UVB. We argue that this is not the main reason for the discrepancies between the proximity effect and other methods.

The actually measured strength of the proximity effect in a single quasar line of sight depends on the UVB, but also on the number of absorption lines present in the "proximity effect zone". That number is generally small, and to first approximation the presence or absence of a line at a given redshift can be described as a Poissonian random process. We have demonstrated that the distribution of the resulting "proximity effect strength" parameter (which directly relates to the UVB) is significantly skewed, even without invoking any physical overdensities. Any direct averaging over a sample of sightlines will inevitably bias the resulting UVB. Only by looking at individual lines of sight separately can this effect be detected and removed.

We proposed and used two different methods of estimating the UVB intensity in the presence of this bias. In the first method, the UVB is taken directly from the mode of the proximity effect strength distribution (PESD). This method is simple and robust against a small number of outliers; on the other hand it is limited to large samples and depends on the condition that the mode is not affected by the outliers. Our second method involves Monte Carlo simulations to calibrate the asymmetry bias of the PESD and then uses straightforward sample averaging, possibly combined with a prior rejection of outliers, and the result is then corrected for the bias. This "hybrid" method is quite stable and works also for smaller samples; it is, however, more complicated to use and depends on a successful removal of outliers.

Our best estimates of the UVB intensity using these two methods give very similar results. The modal estimate is $\log J_{\nu_0} = -21.51 \pm 0.15$, and the hybrid estimator gives $\log J_{\nu_0} = -21.46^{+0.14}_{-0.21}$, which is statistically indistinguishable. This value is in excellent agreement with other methods to estimate or predict the UVB.

If the UV background is known, the data used for the proximity effect can also be employed to reconstruct the absorption pattern without the radiative influence of the quasar. Doing this for our sample of 40 quasars we found that only 10% of them showed very significant excess absorption (by more than a factor of $\sim$3) while most are distributed in a way more or less consistent with Poissonian fluctuations around the cosmic mean absorption expected at these redshifts. Given the widespread notion of quasars residing in massive galaxies, which in turn should sit in massive haloes with significantly clustered environments, this sounds surprising. We have no intention of questioning that picture, and we stress that our measurements constrain exclusively the neutral hydrogen distribution averaged on scales of $\sim$3 proper Mpc towards the quasar.

Nevertheless, our results may bear some relevance to the question of what are the typical halo masses for quasars. Most of the QSOs in our sample are optically selected and therefore presumably radio-quiet, which could mean that their haloes are not exceptionally massive. In a recent paper, Mandelbaum et al. (2008) estimated halo masses of AGN in the Sloan survey from clustering and galaxy-galaxy lensing, finding that optically selected AGN follow the same relation between stellar and halo mass as normal galaxies, whereas radio-loud AGN have much higher halo masses. (Incidentally, the outstanding object in our sample in terms of overdensity is the radio quasar PKS 0237−233; but the next-ranked objects are all optically selected.)

Our argument against significant overdensities of quasars and in favour of the applicability of the proximity effect to measure the UV background gains weight by the excellent agreement between our estimates of the UVB intensity and those obtained by completely different methods. This notion is supported independently by considering the *shape* of the PESD. The observed distribution width clearly favours average densities close to unity; if significant overdensities were involved, a much broader distribution would be expected than the one observed. This additional constraint breaks the degeneracy between UV background and overdensities that has haunted the field for so long.

Finally, we also attempted to constrain the redshift evolution of the UVB intensity. Although the results are still quite uncertain, we could for the first time from a single quasar sample derive useful limits on the amount of evolution. We can rule out at high significance that quasar light dominates the UVB at redshifts $z \gtrsim 4$. Our best fit suggests a mild decrease in the UVB intensity towards higher redshifts, and the derived slope is in astonishingly good agreement with the predictions by Haardt & Madau (2001). Nevertheless, an approximately constant UVB as found by Bolton et al. (2005) and others is also formally consistent with our data.

We have shown that the proximity effect holds the potential to derive important cosmological quantities. While our sample is large in comparison to those of previous studies using high-resolution spectra, it still suffers in several aspects from small number statistics. As the public archives are growing, substantial progress can be expected from applying the proximity effect analysis to further spectra, in particular at higher redshift.

Acknowledgements. We would like to thank ESO for making the ESO data archive publicly available. We also thank Tae−Sun Kim for assisting us in the data reduction process. A.D. and G.W. were partly supported by a HWP grant from the International Helmholtz Institute for Supercomputational Physics. We finally acknowledge support by the Deutsche Forschungsgemeinschaft under Wi 1369/21-1.

References

Agafonova, I. I., Centurión, M., Levshakov, S. A., & Molaro, P. 2005, A&A, 441, 9
Bajtlik, S., Duncan, R. C., & Ostriker, J. P. 1988, ApJ, 327, 570
Bechtold, J. 1994, ApJS, 91, 1
Bechtold, J., Weymann, R. J., Lin, Z., & Malkan, M. A. 1987, ApJ, 315, 180
Bernardi, M., Sheth, R. K., SubbaRao, M., et al. 2003, AJ, 125, 32
Bolton, J. S., Haehnelt, M. G., Viel, M., & Springel, V. 2005, MNRAS, 357, 1178
Carswell, R. F., Whelan, J. A. J., Smith, M. G., Boksenberg, A., & Tytler, D. 1982, MNRAS, 198, 91
Carswell, R. F., Webb, J. K., Baldwin, J. A., & Atwood, B. 1987, ApJ, 319, 709
Cooke, A. J., Espey, B., & Carswell, R. F. 1997, MNRAS, 284, 552
Cristiani, S., D'Odorico, S., Fontana, A., Giallongo, E., & Savaglio, S. 1995, MNRAS, 273, 1016
Dall'Aglio, A., Wisotzki, L., & Worseck, G. 2008, A&A, 480, 359
Davé, R., Hernquist, L., Katz, N., & Weinberg, D. H. 1999, ApJ, 511, 521
Dekker, H., D'Odorico, S., Kaufer, A., Delabre, B., & Kotzlowski, H. 2000, in Optical and IR Telescope Instrumentation and Detectors, Presented at the Society of Photo-Optical Instrumentation Engineers (SPIE), ed. M. Iye, & A. F. Moorwood, Conf. Proc. SPIE, 4008, 534
D'Odorico, V., Bruscoli, M., Saitta, F., et al. 2008 [arXiv:0806.3075]
Ellison, S. L., Hall, P. B., & Lira, P. 2005, AJ, 130, 1345
Espey, B. R. 1993, ApJ, 411, L59
Fardal, M. A., Giroux, M. L., & Shull, J. M. 1998, AJ, 115, 2206
Faucher-Giguère, C.-A., Lidz, A., Hernquist, L., & Zaldarriaga, M. 2008a, ApJ, 682, L9
Faucher-Giguère, C.-A., Lidz, A., Zaldarriaga, M., & Hernquist, L. 2008b, ApJ, 673, 39
Faucher-Giguère, C.-A., Prochaska, J. X., Lidz, A., Hernquist, L., & Zaldarriaga, M. 2008c, ApJ, 681, 831
Fernández-Soto, A., Barcons, X., Carballo, R., & Webb, J. K. 1995, MNRAS, 277, 235
Gaskell, C. M. 1982, ApJ, 263, 79
Giallongo, E., Christiani, S., Fontana, A., & Trèvese, D. 1993, ApJ, 416, 137
Giallongo, E., Christiani, S., D'Odorico, S., Fontana, A., & Savaglio, S. 1996, ApJ, 466, 46
Gnedin, N. Y., Kravtsov, A. V., & Chen, H.-W. 2007, ArXiv e-prints, 707
Guimarães, R., Petitjean, P., Rollinde, E., et al. 2007, MNRAS, 377, 657
Haardt, F., & Madau, P. 1996, ApJ, 461, 20
Haardt, F., & Madau, P. 2001, in Clusters of Galaxies and the High Redshift Universe Observed in X-rays, ed. D. M. Neumann, & J. Tran Thanh Van
Hopkins, P. F., Richards, G. T., & Hernquist, L. 2007, ApJ, 654, 731
Hu, E. M., Kim, T.-S., Cowie, L. L., Songaila, A., & Rauch, M. 1995, AJ, 110, 1526
Hunt, M. P., Steidel, C. C., Adelberger, K. L., & Shapley, A. E. 2004, ApJ, 605, 625
Jena, T., Norman, M. L., Tytler, D., et al. 2005, MNRAS, 361, 70
Kim, T.-S., Cristiani, S., & D'Odorico, S. 2001, A&A, 373, 757
Kim, T.-S., Carswell, R. F., Cristiani, S., D'Odorico, S., & Giallongo, E. 2002, MNRAS, 335, 555
Kim, T.-S., Viel, M., Haehnelt, M. G., Carswell, R. F., & Cristiani, S. 2004, MNRAS, 347, 355
Kim, T.-S., Bolton, J. S., Viel, M., Haehnelt, M. G., & Carswell, R. F. 2007, MNRAS, 382, 1657
Kirkman, D., Tytler, D., Suzuki, N., et al. 2005, MNRAS, 360, 1373
Kulkarni, V. P., & Fall, S. M. 1993, ApJ, 413, L63
Liske, J., & Williger, G. M. 2001, MNRAS, 328, 653
Loeb, A., & Eisenstein, D. J. 1995, ApJ, 448, 17
Lu, L., Wolfe, A. M., & Turnshek, D. A. 1991, ApJ, 367, 19

Lu, L., Sargent, W. L. W., Womble, D. S., & Takada-Hidai, M. 1996, ApJ, 472, 509
Madau, P., Haardt, F., & Rees, M. J. 1999, ApJ, 514, 648
Mandelbaum, R., Li, C., Kauffmann, G., & White, S. D. M. 2008 [arXiv:0806.4089]
McDonald, P., Miralda-Escudé, J., Rauch, M., et al. 2000, ApJ, 543, 1
McDonald, P., Seljak, U., Cen, R., et al. 2005, ApJ, 635, 761
Meiksin, A., & White, M. 2004, MNRAS, 350, 1107
Morton, D. C. 2003, ApJS, 149, 205
Murdoch, H. S., Hunstead, R. W., Pettini, M., & Blades, J. C. 1986, ApJ, 309, 19
Rauch, M. 1998, ARA&A, 36, 267
Rauch, M., Miralda-Escude, J., Sargent, W. L. W., et al. 1997, ApJ, 489, 7
Richards, G. T., Vanden Berk, D. E., Reichard, T. A., et al. 2002, AJ, 124, 1
Rollinde, E., Srianand, R., Theuns, T., Petitjean, P., & Chand, H. 2005, MNRAS, 361, 1015
Sargent, W. L. W., Young, P. J., Boksenberg, A., & Tytler, D. 1980, ApJS, 42, 41
Savaglio, S., Christiani, S., D'Odorico, S., et al. 1997, A&A, 318, 347
Schaye, J., Aguirre, A., Kim, T.-S., et al. 2003, ApJ, 596, 768
Schirber, M., & Bullock, J. S. 2003, ApJ, 584, 110
Schirber, M., Miralda-Escudé, J., & McDonald, P. 2004, ApJ, 610, 105
Scott, J., Bechtold, J., Dobrzycki, A., & Kulkarni, V. P. 2000, ApJ, 130, 67
Scott, J., Bechtold, J., Morita, M., Dobrzycki, A., & Kulkarni, V. P. 2002, ApJ, 571, 665
Shapley, A. E., Steidel, C. C., Pettini, M., Adelberger, K. L., & Erb, D. K. 2006, ApJ, 651, 688
Sokasian, A., Abel, T., & Hernquist, L. 2003, MNRAS, 340, 473
Srianand, R., & Khare, P. 1996, MNRAS, 280, 767
Suzuki, N. 2006, ApJS, 163, 110
Telfer, R. C., Zheng, W., Kriss, G. A., & Davidsen, A. F. 2002, ApJ, 565, 773
Theuns, T., Leonard, A., Efstathiou, G., Pearce, F. R., & Thomas, P. A. 1998, MNRAS, 301, 478
Tytler, D., & Fan, X.-M. 1992, ApJS, 79, 1
Tytler, D., Kirkman, D., O'Meara, J. M., et al. 2004, ApJ, 617, 1
Vanden Berk, D. E., Richards, G. T., Bauer, A., et al. 2001, AJ, 122, 549
Véron-Cetty, M.-P., & Véron, P. 2006, A&A, 455, 773
Weymann, R. J., Carswell, R. F., & Smith, M. G. 1981, ARA&A, 19, 41
Williger, G. M., Baldwin, J. A., Carswell, R. F., et al. 1994, ApJ, 428, 574
Wolf, C., Wisotzki, L., Borch, A., et al. 2003, A&A, 408, 499
Young, P. J., Sargent, W. L. W., Boksenberg, A., Carswell, R. F., & Whelan, J. A. J. 1979, ApJ, 229, 891
Zuo, L. 1993, A&A, 278, 343

Appendix A: Proximity effect on individual lines of sight

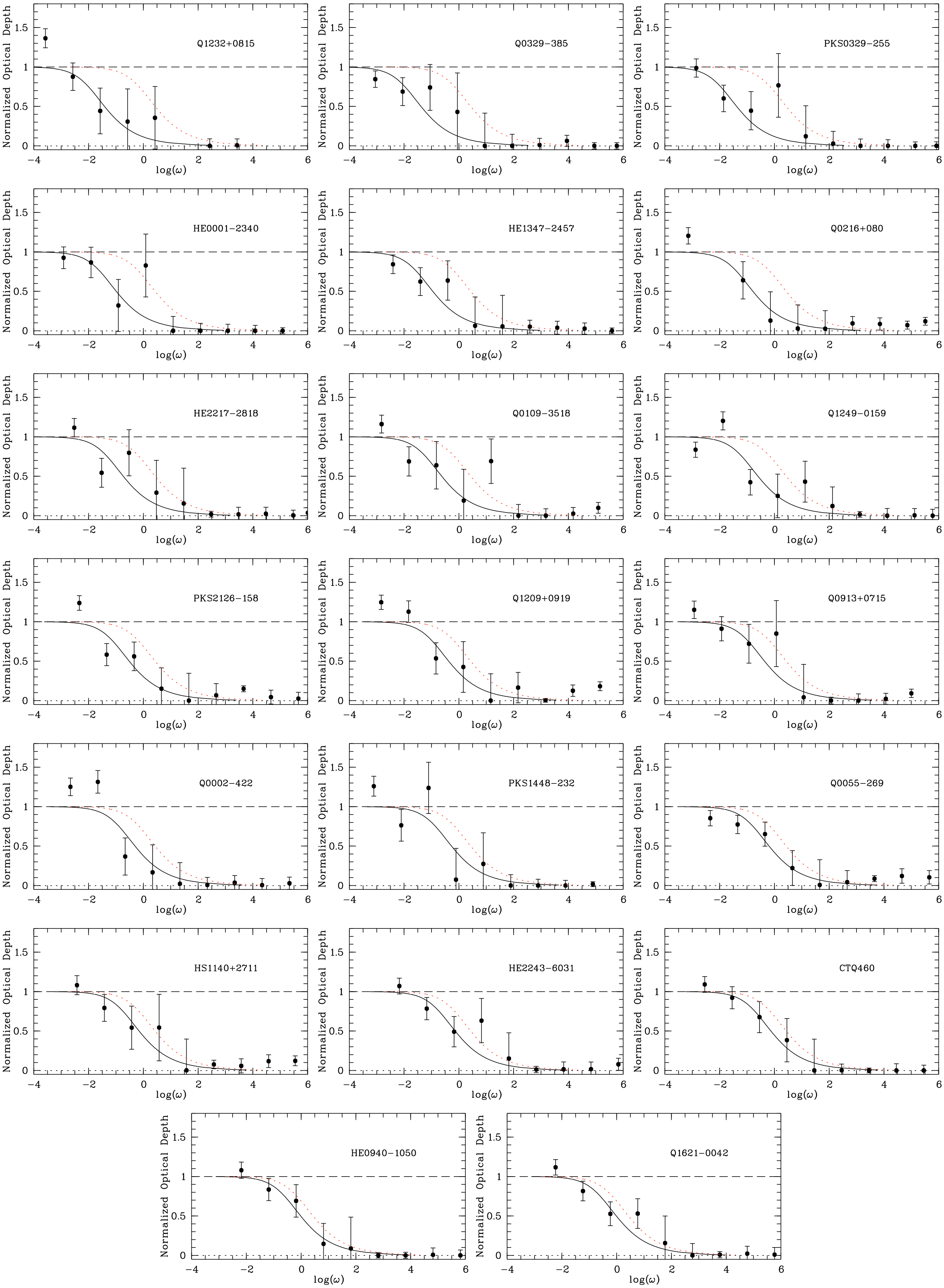

Fig. A.1. The proximity effect signatures in individual lines of sight. Each panel shows the normalised optical depth ξ versus ω, binned in steps of $\Delta \log \omega = 1$, with the best-fit model of the combined analysis superimposed as dotted red lines. The solid lines delineate the best fit to each individual QSO as described in the text.

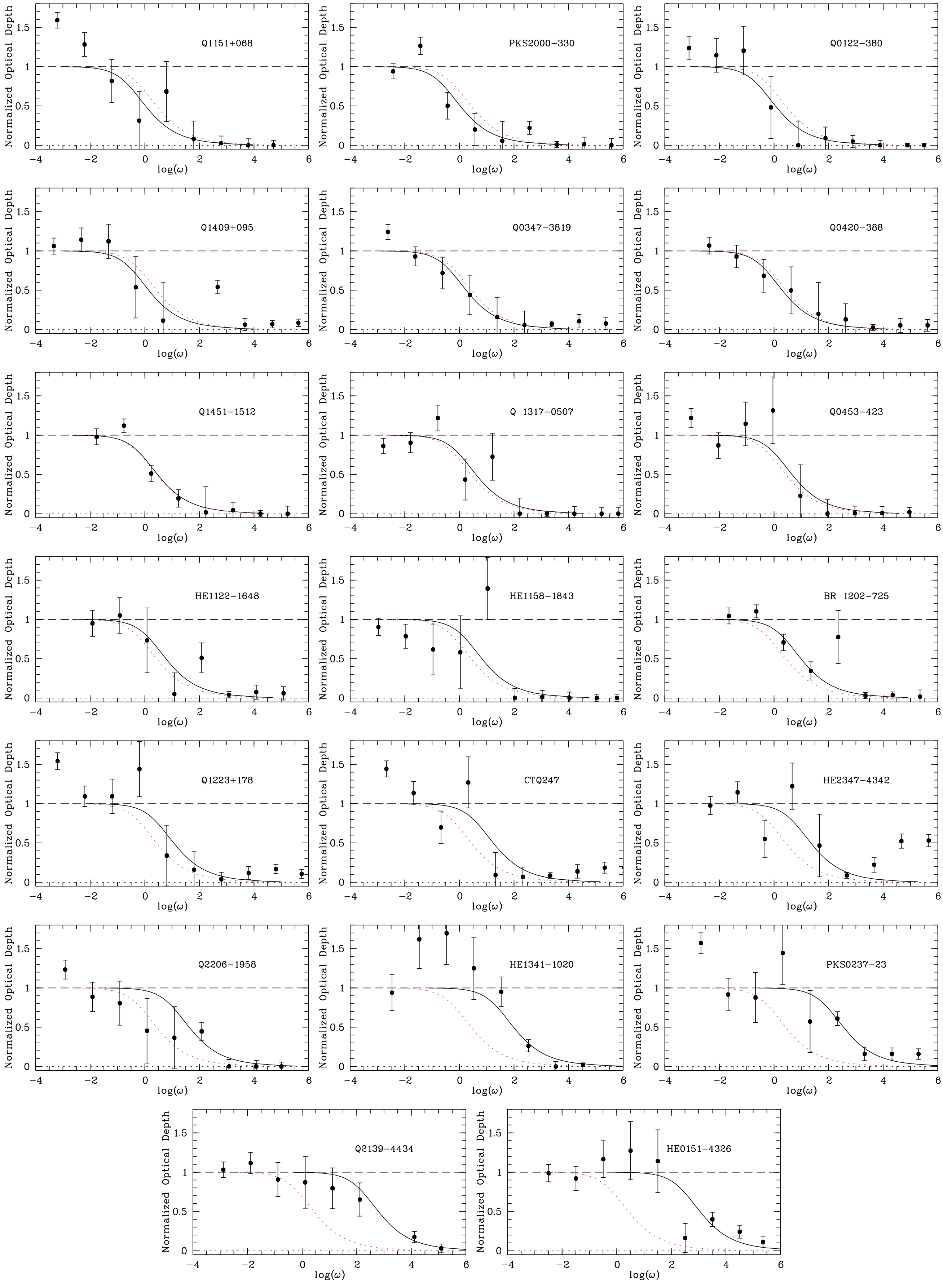

Fig. A.1. continued.